Nonlinear gyrokinetic simulations of microtearing modes in NSTX and NSTX-U-like plasmas

To cite this article before publication: Tajinder Singh *et al* 2026 *Nucl. Fusion* in press https://doi.org/10.1088/1741-4326/aea009

Nonlinear gyrokinetic simulations of microtearing modes in NSTX and NSTX-U–like plasmas

Tajinder Singh[1,*], Tariq Rafiq[1], Eugenio Schuster[1], Cesar Clauser[2], Stanley Kaye[3], Benoit LeBlanc[3]

[1] Department of Mechanical Engineering and Mechanics, Lehigh University, Bethlehem, PA 18015, United States of America

[2] Plasma Science and Fusion Center, Massachusetts Institute of Technology, Cambridge, MA 02139, United States of America

[3]Princeton Plasma Physics Laboratory, Princeton, NJ 08540, United States of America

E-mail: singh@lehigh.edu

March 2026

Abstract. A systematic nonlinear gyrokinetic analysis of microtearing modes (MTMs) in NSTX discharges spanning high-, moderate-, and low-collisionality regimes around mid-radius is presented using the fully electromagnetic code CGYRO. The simulations retain the complete set of perturbed fields, impurity species, equilibrium $\vec{E} \times \vec{B}$ flow shear, and inter-species collisions, yielding electron heat flux predictions in improved agreement with experimental measurements. In the high-collisionality regime, impurity effects are found to play a critical role in reproducing experimentally observed electron heat flux levels. At moderate-collisionality, enhanced zonal flows and fields modify turbulent structures and reduce transport. In the low-collisionality regime, linear analysis reveals coexistence of MTMs and a hybrid ballooning-parity mode; however, nonlinear simulations demonstrate that strong $\vec{E} \times \vec{B}$ shear suppresses hybrid-mode–driven transport, leaving ion heat fluxes near neoclassical levels, consistent with experimental observations. A collisionality scan of the high-collisionality case is further performed to assess NSTX-U–relevant conditions, revealing a transition at lower collisionality in which enhanced zonal flows and fields significantly suppress MTM-driven turbulence and electron heat transport. Sensitivity studies with respect to equilibrium flow shear, temperature and density gradients, electron β, safety factor, and magnetic shear indicate that, at the collisionalities anticipated for NSTX-U, MTMs are expected to contribute to electron heat transport without imposing a dominant confinement constraint. These results provide a nonlinear basis for interpreting collisionality trends in spherical tokamaks and for guiding transport predictions in NSTX-U regimes.

Keywords: spherical tokamaks, turbulent transport, gyrokinetic simulations

1. Introduction

Spherical tokamaks (STs) represent a promising pathway toward viable fusion energy [1]. In this endeavour, turbulent transport driven by micro-instabilities remains a key challenge [2]. Owing to their low aspect ratio, strong plasma shaping, and high-β (the ratio of plasma to magnetic pressure), STs provide a unique setting for the study of turbulent transport, exhibiting confinement properties that differ substantially from those of conventional tokamaks [3]. Their compact configuration improves magnetohydrodynamic (MHD) stability and allows operation at elevated plasma pressures [4]. At the same time, these characteristics produce steep equilibrium gradients, strong magnetic drifts, and increased sensitivity to collisional and electromagnetic effects. Consequently, turbulence in STs can display qualitative differences compared with that observed in high-aspect-ratio tokamaks [5]. In National Spherical Tokamak eXperiment (NSTX) [6] plasmas, these geometric and electromagnetic effects often give rise to hybrid micro-instabilities [7, 8] that do not conform cleanly to classical mode classifications, exhibiting mixed characteristics with significant trapped-electron dynamics.

Microtearing modes (MTMs) [9] are electromagnetic instabilities that play a significant role in driving electron thermal transport in STs [10, 11, 12]. Particularly, previous gyrokinetic studies in NSTX [13, 14] and MAST [15, 16, 17, 18, 19, 20] have demonstrated their relevance in both the core and pedestal regions. In addition, the scaling of MTM-driven transport obtained from the gyrokinetic simulations [21, 22, 23] is broadly consistent with the experimentally observed dependence of the energy confinement time τ_E on collisionality $\nu_\star$ [24, 25, 26], namely $\Omega\tau_E \sim \nu_\star^{-(0.8-0.95)}$, where Ω denotes the ion cyclotron frequency. This consistency suggests that MTMs may play an important role in setting the confinement trends. However, we emphasize that such agreement should not be interpreted as evidence of a causal relationship, as additional turbulence channels could also contribute to the experimentally observed scaling. In this context, the scaling of electron heat flux with collisionality has been studied for electron temperature gradient (ETG) turbulence in MAST using electrostatic local nonlinear gyrokinetic simulations with adiabatic ions [27], where a reduction in electron heat transport due to enhanced zonal flows was observed at low collisionality. The resulting scaling was found to be qualitatively consistent with the experimentally observed scaling of the energy confinement time [21]. Notably, the inferred improvement in confinement at lower collisionality aligns with expectations for future low-collisionality ST regimes, such as those targeted in the upgraded successor of NSTX, NSTX-U [28].

In fact, numerous gyrokinetic studies of NSTX have identified a broad spectrum of micro-instabilities contributing to turbulent transport [10, 22, 23, 13, 14, 29, 30, 31]. These instabilities span spatial scales both larger and smaller than the ion gyroradius, here referred to as ion-scale and electron-scale instabilities, respectively. Ion-scale instabilities include ion temperature gradient (ITG) modes, trapped electron modes (TEMs), kinetic ballooning modes (KBMs), and MTMs, whereas electron-scale turbulence is dominated by ETG modes. While ITG, TEM, and KBM instabilities can drive both ion and electron heat and particle transport, MTMs and ETG modes primarily contribute to electron heat fluxes. Unstable ion-scale modes such as ITG, TEM, and KBM are often suppressed by $\vec{E} \times \vec{B}$ flow shear, leading to ion thermal transport levels close to neoclassical predictions, as observed in high-β H-mode NSTX plasmas [24, 25]. While $\vec{E} \times \vec{B}$ flow shear reduces MTM-driven transport as well, finite transport levels persist over a range of experimentally relevant flow shear values [31].

Consequently, MTMs remain the only ion-scale instability known to drive significant electron thermal transport under these conditions.

In this regard, numerous gyrokinetic studies have investigated MTMs in NSTX [10, 22, 23, 32, 31]. For example, simulations performed with GYRO investigated MTM stability and transport which are found to be strongly sensitive to key plasma parameters, including collisionality, the electron temperature gradient, electron β, and magnetic shear [10, 22, 23]. Similarly, GENE simulations showed that MTMs can dominate the turbulent spectrum in high-β regimes, leading to enhanced electron thermal transport [32]. More recently, CGYRO simulations examined the impact of $\vec{E} \times \vec{B}$ shear on MTM-driven transport [31].

Despite these, a comprehensive understanding of MTM dynamics in NSTX remains incomplete, in part due to modeling simplifications introduced to enable nonlinear saturation or to reduce computational cost, which include the neglect of compressional magnetic field fluctuations, impurity species, and/or $\vec{E} \times \vec{B}$ flow shear [10, 23, 31]. In NSTX, the first nonlinear gyrokinetic simulations of MTMs using GYRO demonstrated that MTMs can drive experimentally relevant levels of electron thermal transport, dominated by magnetic flutter associated with globally stochastic magnetic field lines [10]. However, quantitative agreement with experiment was obtained only in the absence of $\vec{E} \times \vec{B}$ shear; when flow shear was included, the simulated electron heat flux fell well below experimental values [10, 22]. More recently, CGYRO simulations [31] of NSTX investigated the role of $\vec{E} \times \vec{B}$ shear while retaining only the main ion species and thermal electrons, with the ion temperature gradient set to zero, based on the expectation that MTMs are only weakly sensitive to ion temperature drive. These studies achieved agreement with experimental electron heat fluxes only when the flow shearing rate was reduced to half of its experimentally inferred value, although this discrepancy remains within experimental uncertainties. Furthermore, scaling analyses based on nonlinear gyrokinetic simulations [23] exhibit a steeper dependence of electron thermal transport on collisionality and electron temperature gradient compared to predictions from the recently developed neural-network–based electron transport model trained on interpretative analysis results of TRANSP for NSTX [33]. In addition, several open questions persist, including the nonlinear interaction between MTMs and other micro-instabilities such as KBMs and TEMs, as well as their quantitative contributions to transport in reactor-relevant regimes. Resolving these issues is essential for improving predictive models of electron heat transport [34] and for guiding the optimization of operating scenarios in next-generation STs such as NSTX-U.

In this work, we perform a comprehensive linear and nonlinear gyrokinetic analysis of MTMs in NSTX discharges spanning high-, moderate-, and low-collisionality regimes. Unlike earlier nonlinear gyrokinetic studies [10, 23, 31] that neglected compressional magnetic field fluctuations, impurity species, and/or equilibrium flow shear, the present simulations for NSTX cases employ a full-physics model, including all electromagnetic perturbation fields, three kinetic species (thermal deuterium ions, electrons, and carbon impurities), equilibrium $\vec{E} \times \vec{B}$ flow shear, and inter-species collisions. Though some of these physics aspects, particularly $\delta B_{\|}$ fluctuations were included in MAST studies [11]. The nonlinear simulations yield turbulent electron heat fluxes that are in significantly better agreement with experimental measurements than those reported in previous studies [10, 23, 31]. The analysis is further extended by scaling the collisionality of the high-collisionality NSTX case toward values anticipated for NSTX-U, providing a qualitative exploration of MTM-driven transport trends in NSTX-U–relevant regimes rather than a fully self-consistent representation of NSTX-U operating conditions. Nonlinear simulations reveal a transition to a low-collisionality regime in which enhanced zonal flows and fields lead to a more rapid reduction of electron heat transport with decreasing collisionality. Furthermore, sensitivity studies at both high- and low-collisionality are performed with respect to equilibrium flow shear, electron β, electron temperature and density gradients, magnetic shear, and safety factor to assess the potential role of MTMs in future NSTX-U operating scenarios. A rigorous quantitative assessment using dedicated NSTX-U experimental data is left for future work.

The remainder of this paper is organized as follows. Section 2 describes the equilibrium and profile parameters of the low-, moderate-, and high-collisionality NSTX cases studied in this work. The corresponding linear and nonlinear simulation results are presented in Sections 2.1, 2.2, and 2.3, respectively. Section 2.4 summarizes the results for NSTX cases. Section 2.5 presents a scaling analysis of the high-collisionality NSTX case and its extension to NSTX-U–relevant plasma conditions. Finally, conclusions are summarized in Section 3.

2. Linear and nonlinear gyrokinetic analysis of microtearing modes

In this section, we present a detailed linear and nonlinear gyrokinetic analysis of microtearing modes in NSTX discharges spanning high-, moderate-, and low-collisionality regimes. We employ the CGYRO ‡ code [35], which is a fully-electromagnetic, Eulerian gyrokinetic code designed to study microinstabilities, turbulence, and transport in the magnetically confined plasmas using realistic magnetic geometry. Both the linear and nonlinear simulations are performed for the NSTX cases summarized in Table 1. Here, r denotes the midplane minor radius, a the minor radius, Δ' the Shafranov shift, κ the elongation, δ the triangularity, and q the safety factor. The s_κ and s_δ represent the shear of elongation and triangularity, respectively. The magnetic shear is defined as $\hat{s} = \frac{r}{q}\frac{dq}{dr}$, T_i/T_e is the ion-to-electron temperature ratio, and n_{C}/n_e is the density ratio for C^{6+} ions to electrons. The effective electron beta is defined as $\beta_{e,\mathrm{unit}} = \frac{8\pi n_e T_e}{B^2_{\mathrm{unit}}}$, where $B_{\mathrm{unit}} = \frac{q}{r}\frac{d\psi}{dr}$ is the effective magnetic field and the on-axis electron beta is defined as β_e. The generalized MHD parameter is given by $\alpha_{\mathrm{MHD,unit}} = -q^2 R_0 \frac{8\pi}{B^2_{\mathrm{unit}}}\frac{dp}{dr}$, where p is the plasma pressure. The normalized gradient scale lengths are defined as $a/L_{T_e} = -\frac{a}{T_e}\frac{dT_e}{dr}$ for the electron temperature, a/L_{n_e} for the electron density, a/L_{T_i} for the ion temperature, and a/L_{n_i} for the ion

‡ CGYRO version (git commit) employed for simulations is `29268b4b4`.

density. Similarly, a/L_{T_C} and a/L_{n_C} are the normalized gradient scale lengths for temperature and density of C^{6+} impurity ions. The effective plasma charge is denoted by Z_{eff}, and the electron–ion collisionality (in units of c_s/a) is defined as $\nu^{e/i} = \nu_{ei} Z_{\text{eff}}$, where $\nu_{ei} = 4\pi n_e e^4 \log\Lambda/(2T_e)^{3/2} m_e^{1/2}$ is the collision frequency coefficient, $\log\Lambda$ is the Coulomb logarithm, e and m_e are the charge and mass of electron, and $c_s = \sqrt{T_e/m_D}$ is the ion sound speed, where m_D is the mass of deuterium. The perpendicular ($\vec{E}\times\vec{B}$) flow shear is defined as $\gamma_E = \frac{r}{q}\frac{d\omega_0}{dr}$ (in units of c_s/a), where $\omega_0 = -\frac{d\Phi_0}{d\psi}$ is the toroidal rotation frequency, Φ_0 is the equilibrium electric potential, and ψ is the poloidal flux. The Mach number is defined as $M = \frac{v_{\text{tor}}}{c_s} = \frac{R\omega_0}{c_s}$, and the parallel flow shear is given by $\gamma_P = R\frac{d\omega_0}{dr} = q\frac{R}{r}\gamma_E$, also in units of c_s/a. The Miller representation [36, 37] is used to describe the local equilibrium parameters at the chosen radial location. It is important to note that, unlike the temperature profiles, the electron density profile shows pronounced "ears" that appear shortly after the L-to-H transition, suggesting the formation of an edge particle transport barrier associated with electron density accumulation at the plasma boundary due to carbon fueling at the edge [38]. Consequently, this leads to a region of negative electron density gradient. The linear gyrokinetic analysis of these discharges is also presented in Refs. [39, 40]. The selected scenarios are chosen such that no unstable electron-scale modes, such as ETG modes, are present, as confirmed by the linear gyrokinetic analysis. Under these conditions, MTMs are expected to be the primary drivers of the experimentally observed electron thermal transport. Furthermore, fast ions generated by beam heating are not included in the gyrokinetic analysis because their density is very low ($n_{\text{fast}}/n_e \sim (0.1$–$0.5)\%$) at the radial locations analyzed in NSTX cases, suggesting a negligible impact on MTM dynamics [22].

2.1. High-collisionality case

We begin by examining the high-collisionality NSTX case, followed by moderate- and low-collisionality cases to elucidate the evolution of MTM stability, nonlinear saturation, and transport across collisionality. Figure 1 shows the variation of the linear growth rates and real frequencies as a function of the normalized binormal wavenumber $k_\theta\rho_s$, where $\rho_s = \sqrt{m_D T_e}/B_{\text{unit}}$. Though ρ_s is defined using CGYRO convention, the magnetic field normalization enters both k_θ and ρ_s in a compensating manner, such that $k_\theta\rho_s$ remains invariant of the definition of magnetic field [41]. The linear simulations use numerical resolutions of $n_\theta = 64$, $n_r = 8$, $n_\epsilon = 8$, $\epsilon^2_{\text{max}} = 8$, and $n_\xi = 24$, where n_r and n_θ represent the grid points in the radial and parallel directions, respectively, n_ϵ is the energy grid points, ϵ_{max} is the maximum energy, and n_ξ represents the number of Legendre pseudo-spectral grid points in the pitch-angle space. All the simulations presented for NSTX cases are performed using the Sugama collision operator for multi-species collisions, which is valid for arbitrary wavelengths. The resulting spectrum is dominated by modes propagating in the electron diamagnetic direction, as indicated by the negative real frequencies. A parity analysis of the parallel vector potential, shown in Fig. 2, confirms that these modes exhibit tearing parity and can therefore be identified

Table 1. Summary of the relevant equilibrium and profile parameters at the analyzed radial locations of the NSTX discharges.

Quantity	High-collisionality	Moderate-collisionality	Low-collisionality
Discharge shot #	120968 @560 ms	129016 @490 ms	120982 @620 ms
TRANSP RUN ID	120968A02	129016A03	120982A09
r/a	0.60	0.50	0.60
R/a	1.53	1.53	1.60
Δ'	-0.29	-0.22	-0.36
κ	1.71	1.40	2.20
δ	0.13	0.13	0.24
s_κ	0.12	-0.01	0.03
s_δ	0.17	0.11	0.22
q	1.71	1.28	2.97
$\hat{s}$	1.70	0.44	0.97
T_e (eV)	463.30	638.70	922.10
T_i/T_e	0.94	1.20	1.15
T_{C}/T_e	0.95	1.20	1.15
n_e ($\times 10^{19}$ m^3)	5.96	5.33	5.53
n_i/n_e	0.63	0.91	0.84
n_{C}/n_e (%)	6.24	1.54	2.61
$\beta_{e,\mathrm{unit}}$ (%)	2.51	2.93	1.17
β_e (%)	8.65	5.67	6.69
$\alpha_{\mathrm{MHD,unit}}$	0.41	0.14	0.54
a/L_{T_e}	2.66	1.67	1.59
a/L_{n_e}	-0.77	-0.41	-0.93
a/L_{T_i}	2.45	0.87	2.86
a/L_{n_i}	0.71	-0.31	-0.13
$a/L_{T_{\mathrm{C}}}$	2.46	0.92	2.85
$a/L_{n_{\mathrm{C}}}$	-3.26	-1.41	-5.22
Z_{eff}	2.87	1.46	1.78
$\nu^{e/i}$	3.91	1.34	0.58
γ_E	0.17	0.59	0.30
M	-0.22	-0.62	-0.43
γ_P	-0.76	-2.29	-2.34

as MTMs. In addition, the field-line tearing parameter is employed as a quantitative diagnostic to further distinguish MTMs, similar to Ref. [20, 31], and is defined as follows:

$$C_{\rm tear} = \frac{|\int \delta A_\parallel {\rm d}l|}{\int |\delta A_\parallel| {\rm d}l}. \tag{1}$$

The parameter $C_{\rm tear}$ provides a quantitative measure of the parity of $\delta A_\parallel$ along the field line. Since MTMs are associated with magnetic reconnection at rational surfaces, their parallel vector potential exhibits predominantly even (tearing) parity, resulting in $C_{\rm tear}$ values close to unity. In contrast, ballooning modes possess predominantly odd parity, leading to smaller values of $C_{\rm tear}$. For the modes shown in Fig. 1, the field-line tearing parameter satisfies $C_{\rm tear} > 0.9$, quantitatively confirming their identification as MTMs. Although the dominant parity of the eigenfunction in Fig. 1 can be readily identified by visual inspection, $C_{\rm tear}$ provides an objective and reproducible diagnostic that is particularly useful for parameter scans and cases where the eigenfunctions exhibit mixed parity or become noisy, making visual classification less straightforward. We also emphasize that $C_{\rm tear} > 0.9$ is not a strict threshold separating tearing- and ballooning-parity modes, but rather an empirical criterion used to identify modes with predominantly MTM-like character. The sensitivity of the linear spectrum to parallel magnetic field fluctuations, $\delta B_\parallel$, and to the presence of C^{6+} impurities is also examined, which was ignored in the previous work [31]. The weak dependence of both the growth rates and real frequencies on $\delta B_\parallel$ reflects the fact that MTMs are driven primarily by electron temperature gradients and collisional tearing-parity perturbations in $\delta A_\parallel$, with $\delta B_\parallel$ playing only a secondary role in their linear dynamics, consistent with the earlier findings [15, 22]. In contrast, the inclusion of C^{6+} impurities leads to an increase in both the maximum growth rate and the width of the unstable spectrum. This behavior arises from the combined destabilizing effect of impurities due to (i) an increased electron–ion collisionality and (ii) the nearly adiabatic response of impurity ions which shield the electrostatic potential fluctuations [23]. The adiabatic effect of impurities results in shielding of the electrostatic potential response through a nearly adiabatic ion response, ($\delta n_i/n_i \approx Z_{\rm eff}\delta\phi/T_i$). This shielding reduces the electrostatic response that would otherwise partially stabilize the tearing-layer dynamics, thereby favoring MTM growth [42, 43]. Although some studies have reported destabilizing [15] or negligible [17] effects of the electrostatic potential on MTMs as well. In the present work, impurities are retained gyrokinetically, which ensures a self-consistent treatment of collisional and electromagnetic effects and allows quantifying their influence on MTM stability. This treatment avoids imposing adiabaticity a priori and retains the possibility of non-adiabatic impurity dynamics should they become important in other parameter regimes. We note, however, that the precise mechanism by which impurity shielding modifies MTM stability has not been isolated in the present work and would require a dedicated study. Recent GENE simulations [32] also indicate that impurity content can significantly modify MTM stability even in regimes with strong electromagnetic fluctuations. The resulting broadening of the unstable spectrum has important implications for nonlinear transport, as it increases the range of k_θ that contributes to the electron heat flux. It is important to note that the effect of impurity species on MTM linear stability and nonlinear transport is different from the other instabilities such as ITG and TEM, where the impurity leads to a reduction in the linear growth rates as well as the associated nonlinear transport due to dilution effect or an increase in the zonal flow [44, 45].

Figure 2 presents the eigenfunctions of the perturbed fields for the most unstable MTM at the normalized wavenumber $k_\theta \rho_s = 1.0$, with each quantity normalized to the maximum value of $\delta\phi$. The electrostatic potential exhibits odd parity with respect to the ballooning angle θ, while the parallel vector potential, $\delta A_{||}$, displays even parity, consistent with the characteristic tearing parity of MTMs. This parity structure clearly distinguishes MTMs from other electromagnetic instabilities, such as KBMs, which exhibit ballooning parity. The eigenfunction of $\delta B_{||}$ remains small in amplitude compared to that of $\delta A_{||}$, further confirming its secondary role in the linear dynamics of MTMs.

Regarding the parity of $\delta B_{||}$, unlike $\delta A_{||}$, whose tearing parity is a defining characteristic of MTMs, the parity of $\delta B_{||}$ is not typically used as a mode-identification criterion as MTMs are largely insensitive to $\delta B_{||}$ fluctuations. The observed odd parity of $\delta B_{||}$ can be understood qualitatively from the perpendicular pressure-balance relation,

$$\delta p_\perp + \frac{B_0 \delta B_{||}}{\mu_0} \simeq 0,$$

which gives

$$\frac{\delta B_{||}}{B_0} \simeq -\frac{\mu_0 \delta p_\perp}{B_0^2}.$$

Thus, the symmetry of $\delta B_{||}$ is closely linked to the symmetry of the pressure perturbation. For a tearing-parity MTM, the electromagnetic perturbations possess a definite symmetry about the rational surface. If the associated pressure perturbation is antisymmetric, perpendicular pressure balance requires $\delta B_{||}$ to also be antisymmetric, resulting in odd parity. More generally, the parity of $\delta B_{||}$ arises from its coupling to the tearing-parity electromagnetic eigenfunction through Ampère's law and pressure-balance relations. However, the detailed parity structure of $\delta B_{||}$ has not been investigated in the present work, and a rigorous explanation would require a dedicated analysis.

Following the linear analysis, we perform nonlinear gyrokinetic simulations of the NSTX high-collisionality case. The nonlinear simulations use $n_\theta = 32$, $n_\epsilon = 8$, $\epsilon^2_{\max} = 8$, $n_\xi = 16$, 512 radial (k_x) grid points with $k_{x,\min}\rho_s = 0.044$, 32 binormal (k_y) grid points with $k_{y,\min}\rho_s = 0.033$. These simulation parameters result in the domain size $(L_x, L_y) \approx (142, 190)\rho_s$, perpendicular to the field-line. Nonlinear gyrokinetic studies of MTM-driven turbulence are computational challenging and require high numerical resolution to properly resolve the MTMs, as compared to the instabilities such as ITG, especially in the radial direction [11]. Therefore, simulations presented in this work use small $k_{x,\min}\rho_s$ to precisely capture the nonlinear dynamics of MTMs. Figure 3 shows the time evolution of the electron heat flux, normalized to the gyro-Bohm heat flux, illustrating the effects of $\delta B_\parallel$ fluctuations and C^{6+} impurities, as well as the nonlinear electron heat-flux spectrum as a function of the normalized wavenumber $k_\theta\rho_s$ for the case including both $\delta B_\parallel$ and C^{6+}. The experimentally inferred electron heat flux is $Q_e^{\exp} = (3\text{–}4)Q_{\rm GB}$, calculated from the power balance studies using TRANSP [46], where $Q_{\rm GB} = c_s n_e T_e(\rho_s/a)^2$. The uncertainty in the heat flux primarily arises from experimental uncertainties in measured plasma profiles and heating power deposition, which propagate through the power balance calculation. The simulations yield $Q_e = (3.36 \pm 0.32)Q_{\rm GB}$, reproducing the experimental electron heat flux only when C^{6+} impurities are included. Whereas the turbulent ion heat flux due to MTMs remain considerably small; $Q_i = (0.055 \pm 0.005)Q_{\rm GB}$. By contrast, parallel magnetic field fluctuations, $\delta B_\parallel$, are found to have a negligible impact on the turbulent transport. Simulations retaining only two kinetic species (thermal deuterium ions and electrons), thereby excluding impurity-driven enhancements of collisionality, produce significantly lower electron heat fluxes, $Q_e = (1.58 \pm 0.16)Q_{\rm GB}$, underscoring the critical role of impurities on MTM-driven transport. These results show improved agreement with experimental measurements compared to previous studies [10, 31]. The nonlinear electron heat-flux spectrum peaks at $k_\theta\rho_s \sim 0.1$, while ion heat fluxes remain much smaller than the electron heat fluxes ($Q_i \ll Q_e$). Extensive convergence tests (see Appendix A) confirm that these results are robust with respect to numerical resolution. It is also worth mentioning here that the nonlinear simulation presented here do not fully resolve the whole linear spectrum of MTMs which extend up to $k_\theta\rho_s \sim 1.6$. In Appendix A, we present convergence tests to assess the adequacy of the spectral resolution. As shown in Fig. A1, extending $k_{\theta,\max}\rho_s \sim 1$ to $k_{\theta,\max}\rho_s \sim 2$ yields nearly identical electron heat transport levels, demonstrating that the simulations presented here are well converged with respect to the maximum resolved binormal wavenumber. It is also important to note that the nonlinear electron heat flux spectrum (Fig. 3b) peaks at $k_\theta\rho_s \sim 0.1$, corresponding to the dominant energy injection scale of the turbulence, which lies well below the adopted cut-off $k_{\theta,\max}\rho_s \sim 1$. Energy cascades toward higher wavenumbers where it is dissipated, and the convergence tests indicate that resolving modes up to $k_{\theta,\max}\rho_s \sim 1$ is sufficient to capture the dissipation range without affecting the resulting transport levels.

Figure 4 shows contour plots of the perturbed electrostatic potential, $\delta\phi$, parallel vector potential, $\delta A_\parallel$, and parallel magnetic field $\delta B_\parallel$ on the outer midplane ($\theta = 0$) during the nonlinear saturated phase. The $\delta\phi$ fluctuations exhibit relatively small-scale eddies with limited radial extent, whereas $\delta A_\parallel$ develops elongated structures spanning a large fraction of the flux-tube width. The $\delta B_\parallel$ fluctuations are relatively much smaller than the $\delta A_\parallel$ fluctuations, in accordance with the linear analysis. Such features are characteristic of MTM turbulence, in which magnetic perturbations dominate over electrostatic fluctuations and drive enhanced electron transport through magnetic flutter. The presence of these extended $\delta A_\parallel$ structures implies strong parallel

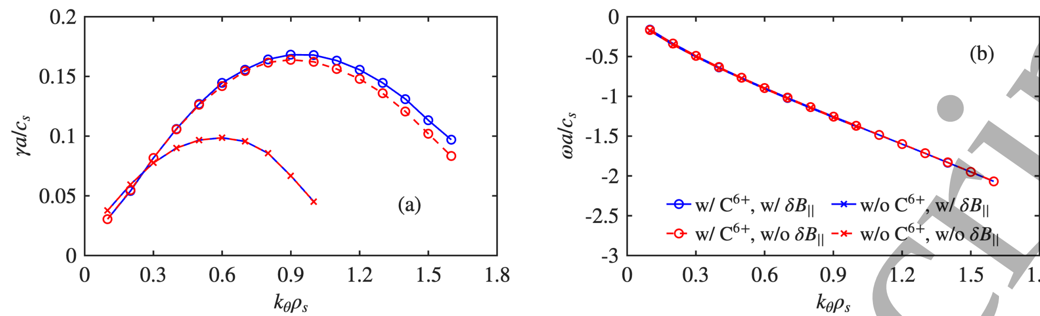

Figure 1. Linear analysis of the high-collisionality case. (a) Growth rates γ and (b) real frequencies ω versus normalized wavenumber $k_\theta \rho_s$. The effects of parallel magnetic field fluctuations $\delta B_\parallel$ and C^{6+} impurities on the linear spectrum are also shown.

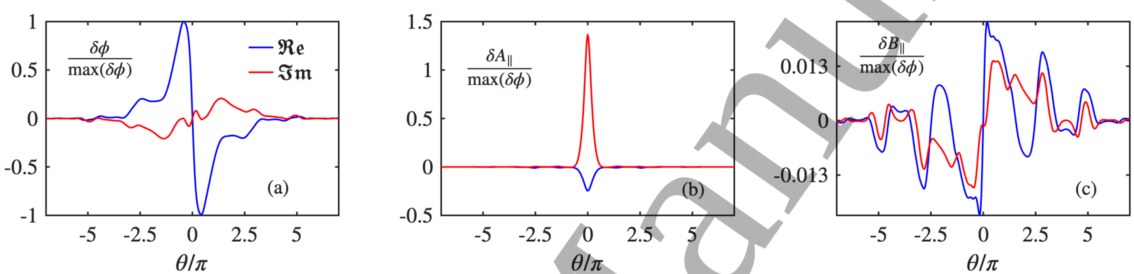

Figure 2. Eigenfunctions (a) $\delta\phi$, (b) $\delta A_\parallel$, and (c) $\delta B_\parallel$ as a function of the ballooning angle for $k_\theta \rho_s = 0.9$ for the high-collisionality case. The values are normalized by the $\max(\delta\phi)$.

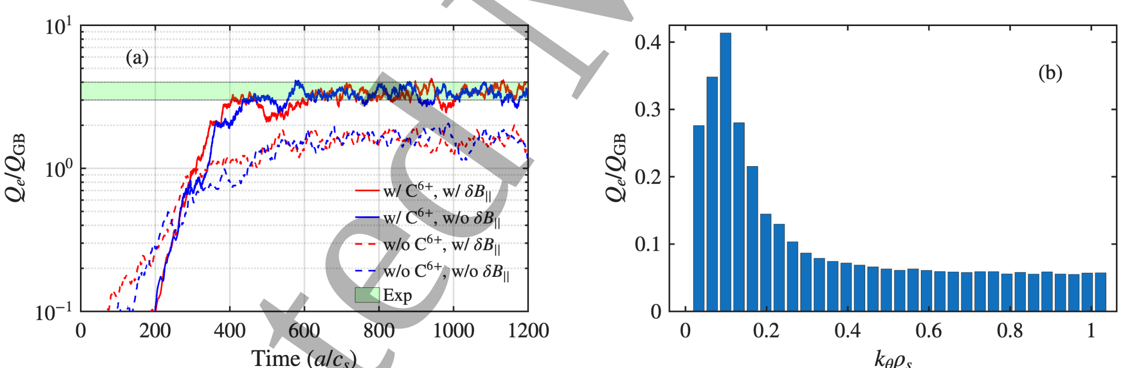

Figure 3. Nonlinear simulation results for the high-collisionality case. (a) Time evolution of the electron heat fluxes normalized to the gyro-Bohm value $Q_{\rm GB}$, illustrating the effects of $\delta B_\parallel$ fluctuations and C^{6+} impurities. (b) Spectrum of normalized electron heat flux versus $k_\theta \rho_s$ for the case with $\delta B_\parallel$ fluctuations and C^{6+} impurities.

connectivity and stochasticity of magnetic field lines, consistent with the MTM-driven transport levels shown in Fig. 3. To verify numerical robustness, the simulations were repeated using half of the original radial domain, yielding unchanged heat fluxes. This confirms that the elongated structures are physical in origin rather than numerical artifacts (see Appendix A).

MTMs generate magnetic perturbations that locally (in the vicinity of rational surfaces) distort magnetic flux surfaces and can lead to the formation of magnetic islands. When such perturbations become sufficiently strong and overlap, they may

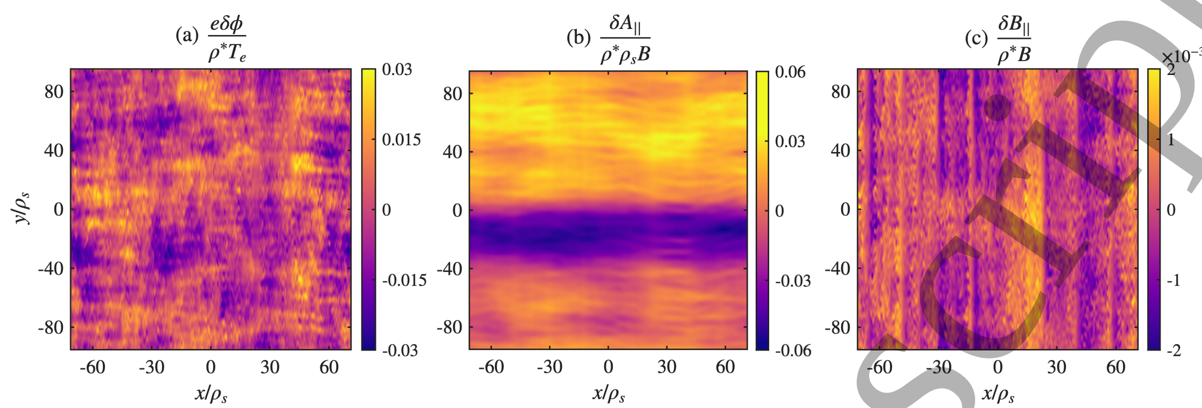

Figure 4. Contour plots of (a) $\delta\phi$ and (b) $\delta A_\parallel$, and (c) $\delta B_\parallel$ on the outer midplane at $\theta = 0$ in the nonlinear phase of the simulation for the high-collisionality case, where $\rho^* = \rho_s/a$.

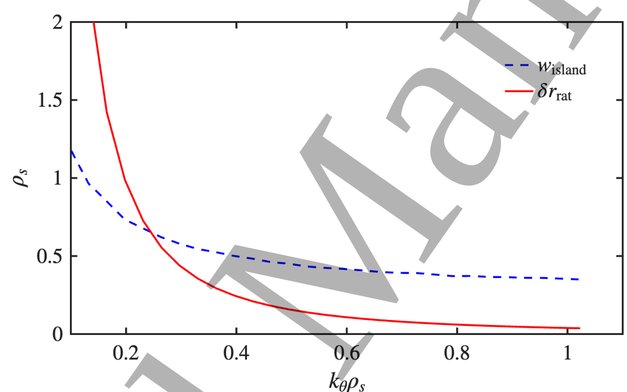

Figure 5. Estimated island width ($\mathrm{w_{island}}$) and the spacing between rational surfaces (δr_{rat}) from the nonlinear phase of the simulation for the high-collisionality case.

produce regions of stochastic magnetic field lines [47]. In both cases, electron heat transport can be enhanced through rapid parallel streaming along perturbed field lines [48]. This class of transport is commonly referred to as magnetic flutter transport. To quantify the onset and significance of such magnetic perturbations in the present simulations, we examine the size of the resulting magnetic islands relative to the spacing between neighboring rational surfaces.

Figure 5 shows the magnetic island width, $\mathrm{w_{island}}$, together with the spacing between adjacent rational surfaces, estimated from the saturated phase of the nonlinear simulations, as a function of the normalized wavenumber $k_\theta \rho_s$. The magnetic island width associated with the reconnection of resonant modes at a rational surface $q = m/n$ is evaluated following the standard expression given in Ref. [49]:

$$\mathrm{w_{island}} = 4\sqrt{\frac{\delta B}{B}\frac{rR}{n\hat{s}}}, \tag{2}$$

where m and n are the poloidal and toroidal mode numbers, respectively. To calculate the island width from Eq. (2), $\delta B/B$ as a function of n is used rather than a constant

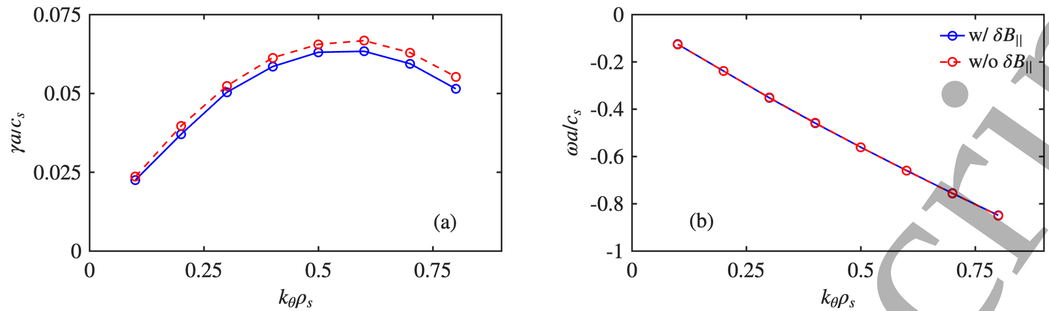

Figure 6. Linear analysis of the moderate-collisionality case. (a) Growth rates γ and (b) real frequencies ω versus normalized wavenumber $k_\theta\rho_s$ with C^{6+} impurity ions included in the simulations. The influence of parallel $\delta B_{\|}$ fluctuations on the linear spectrum is also included.

value for all n. The spacing between two rational surfaces with consecutive m and the same n is given by:

$$\Delta r \simeq \frac{1}{nq'} = \frac{r}{nq\hat{s}}. \tag{3}$$

In a local nonlinear gyrokinetic simulation resolving toroidal mode numbers $[n_0, 2n_0, \ldots, Nn_0]$, the minimum spacing between adjacent rational surfaces corresponding to two largest n on the grid at constant m is given by [50]:

$$\delta r_{\mathrm{rat}} \approx \frac{n_0 r}{n^2 q\hat{s}}. \tag{4}$$

When the magnetic island width exceeds the spacing between rational surfaces, the magnetic field lines become stochastic [47], thereby providing an effective mechanism for electron thermal transport [48]. The island overlap criteria $\mathrm{w}_{\mathrm{island}} > \delta r_{\mathrm{rat}}$ has also previously been used to indicate the onset of stochastic transport [10, 23, 56]. The value of the ratio $\mathrm{w}_{\mathrm{island}}/\delta r_{\mathrm{rat}}$ reported at $k_{\theta,\max}$, is taken simply to indicate a level of stochasticity attained within the resolved turbulence spectrum. In the present simulations, the island overlap criterion, $\mathrm{w}_{\mathrm{island}} > \delta r_{\mathrm{rat}}$, is satisfied for $k_\theta\rho_s > 0.24$, with the ratio $\mathrm{w}_{\mathrm{island}}/\delta r_{\mathrm{rat}}$ reaching approximately 9.5 at the highest normalized wavenumber. This extensive overlap leads to enhanced electron thermal transport via stochastic magnetic field lines.

2.2. Moderate-collisionality case

In contrast to the high-collisionality case, the moderate-collisionality scenario exhibits lower collisionality and stronger flow shear, as summarized in Table 1. The simulations include all three kinetic species: thermal deuterium ions, electrons, and fully-ionized carbon impurity ions. To identify the dominant instabilities, linear simulations are performed using the same numerical resolution as in the high-collisionality case, except with $n_r = 16$. The linear spectrum is shown in Fig. 6. The linear analysis reveals a spectrum entirely dominated by MTMs propagating in the electron diamagnetic direction, characterized by negative real frequencies and the tearing parity in parallel magnetic potential as shown in Fig. 7. The field-line tearing parameter for the unstable modes is $C_{\text{tear}} > 0.9$, further confirming the identification as MTMs. Parallel magnetic fluctuations, $\delta B_{\|}$, remain small compared to $\delta A_{\|}$, indicating their negligible influence on linear stability. These results demonstrate that MTMs persist as the dominant linear instability, albeit with reduced drive relative to the high-collisionality regime.

For the nonlinear simulations, the same numerical setup as in the high-collisionality case is used, except for 480 radial (k_x) grid points with $k_{x,\min}\rho_s = 0.014$ and 32 binormal (k_y) grid points with $k_{y,\min}\rho_s = 0.05$ are used. These simulation parameters lead to a domain size $(L_x, L_y) \approx (454, 126)\rho_s$, perpendicular to the field-line. Figure 8 shows the time evolution of the electron heat flux, normalized to the gyro-Bohm value, highlighting the effect of $\delta B_{\|}$ fluctuations, along with the nonlinear electron heat-flux spectrum as a function of $k_\theta\rho_s$ for the case including these fluctuations. The saturated electron heat flux reaches $Q_e = (1.14 \pm 0.08)Q_{\text{GB}}$, in close agreement with the experimental estimate $Q_e^{\exp} = (1-2)Q_{\text{GB}}$ from power balance studies using TRANSP, validating the model fidelity in this regime. The turbulent ion heat flux driven by MTMs remain small; $Q_i = (0.007 \pm 0.002)Q_{\text{GB}}$. Consistent with the linear results, $\delta B_{\|}$ fluctuations have a negligible effect on transport. The nonlinear spectrum peaks at $k_\theta\rho_s \sim 0.25$. The stronger zonal flows and zonal fields characteristic of this case modify the turbulent eddies (Fig. 9), breaking their radial extent while elongating them in the binormal direction, thereby suppressing transport relative to the high-collisionality case. Extensive convergence tests (see Appendix B) confirm the robustness of these results with respect to numerical resolution and domain size.

Figure 9 shows contour plots of the $\delta\phi$ and $\delta A_{\|}$ fluctuations on the outer midplane ($\theta = 0$). The $\delta B_{\|}$ fluctuations are relatively much smaller than the $\delta A_{\|}$ fluctuations, in accordance with the linear analysis; therefore, not shown here. In this moderate-collisionality case, the turbulence is characterized by fragmented eddies together with relatively strong zonal flows and zonal fields. To display the non-zonal turbulent structures more clearly, the zonal ($k_y = 0$) components have been removed from the fluctuating quantities shown in Fig. 9 during post-processing. Retaining these components produces structures that appear extended in the binormal direction. MTMs are known to saturate via zonal flows/fields, with zonal fields particularly playing a special role in their nonlinear saturation [51, 11], whereas electrostatic instabilities, such as ITG, saturate primarily through zonal flows [52]. Zonal flows/fields disrupt radially extended structures and thereby reduce cross-field transport. Compared with the high-collisionality case, the $\delta A_{\|}$ fluctuations occupy a narrower radial extent, consistent with the lower electron heat fluxes shown in Fig. 8. In CGYRO simulations, the radial domain size is defined as $L_x = j/(\hat{s}k_{y,\min})$, where j is the integer determining the number of rational flux surfaces of the lowest finite toroidal mode number to be accommodated. Therefore, due to the small magnetic shear and the small minimum binormal wavenumber, $k_{y,\min}\rho_s$, the radial extent of the flux-tube domain can become comparable to or exceed the physical size of the plasma, potentially questioning the validity of the local approximation. Nevertheless, the simulations remain informative for identifying the dominant linear instabilities and their characteristic mode structures, which are largely insensitive to the precise radial extent of the flux-tube domain, although global gyrokinetic simulations may be required for a fully quantitative description of the turbulence in this regime.

Figure 10 shows the magnetic island width, $\mathrm{w_{island}}$, along with the spacing between rational surfaces, estimated from the saturated phase of the nonlinear simulations, as a function of the normalized wavenumber $k_\theta \rho_s$. The island overlap criterion, $\mathrm{w_{island}} > \delta r_{\mathrm{rat}}$, is satisfied for $k_\theta \rho_s > 0.97$, with the ratio $\mathrm{w_{island}}/\delta r_{\mathrm{rat}}$ reaching approximately 1.96 at the highest wavenumber. Compared to the high-collisionality case, where this ratio reaches values of order ~ 10 and indicates extensive island overlap, the smaller value observed here reflects a more marginal overlap and a reduced degree of magnetic field line stochasticity. This partial overlap nonetheless produces stochastic magnetic field lines, providing a mechanism for electron thermal transport in this regime, albeit at reduced levels relative to the high-collisionality case.

2.3. Low-collisionality case

Low-collisionality NSTX cases are particularly relevant, as NSTX-U plasmas are expected to operate in this regime. The simulations discussed here include fully-ionized carbon impurity ions along with thermal deuterium ions and electrons. Linear simulations are performed to identify the unstable modes using a resolution same as that of high-collisionality case except with $n_\theta = 48$, $n_r = 12$. The results, summarized in Fig. 11, show the growth rates and real frequencies as a function of $k_\theta \rho_s$. The spectrum reveals the simultaneous presence of modes propagating in both the electron and ion diamagnetic directions. Modes in the electron diamagnetic direction are identified as MTMs, confirmed by the field-line tearing parameter $C_{\mathrm{tear}} > 0.9$. In contrast, low-k_y modes ($k_y \rho_s < 0.2$) propagating in the ion diamagnetic direction exhibit ballooning parity and a significant normalized parallel electric field component, which is calculated as follows:

$$\hat{E}_\parallel = \frac{\int \mathrm{d}z |-\partial_z \delta\phi + i\omega\delta A_\parallel|}{\int \mathrm{d}z |\partial_z \delta\phi| + |i\omega\delta A_\parallel|}. \tag{5}$$

This parallel electric field, $\hat{E}_\parallel$, serves as a measure of the ideal-MHD character of the mode [53], where z is the coordinate along the magnetic field line. For KBMs, parallel electric field is vanishingly small; $\hat{E}_\parallel < 0.1$. Moreover, the modes gradually transition to pure TEM or pure KBM as the electron or ion temperature gradients are increased, respectively, which are the primary drives for these instabilities. On the basis of these characteristics, the modes are referred to as hybrid modes. The effect of $\delta B_\parallel$ fluctuations on linear stability is also examined. While MTM growth rates and frequencies are largely insensitive to $\delta B_\parallel$, neglecting these fluctuations stabilizes hybrid modes, consistent with the known role of compressional magnetic perturbations in ballooning-mode physics [54]. This contrast highlights a fundamental difference between the two instabilities:

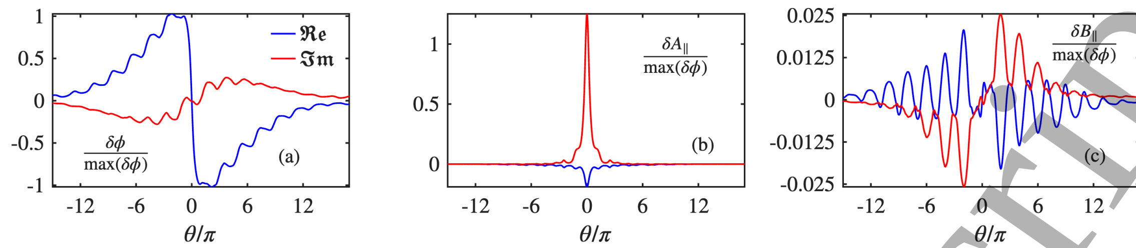

Figure 7. Eigenfunctions (a) $\delta\phi$, (b) $\delta A_{\|}$, and (c) $\delta B_{\|}$ as a function of the ballooning angle for $k_\theta\rho_s = 0.6$ for the moderate-collisionality case. The values are normalized by the $\max(\delta\phi)$.

MTMs are primarily driven by collisional tearing-parity dynamics associated with $\delta A_{\|}$, whereas hybrid modes require $\delta B_{\|}$ to satisfy perpendicular pressure balance and remain unstable. The coexistence of MTMs and hybrid modes in the low-collisionality regime makes this scenario particularly relevant for NSTX-U, where flow shear is expected to strongly influence which instability dominates transport. Additionally, this case has the highest q value among all NSTX cases considered in this work. The observations are qualitatively consistent with recent results in STEP [55], where strong electromagnetic turbulence driven by hybrid modes (h-KBMs) has been reported at high q conditions.

To further characterize the linearly unstable modes, we analyzed the eigenfunctions of the perturbed fields. Figure 12 shows these eigenfunctions, each normalized to the maximum value of $\delta\phi$, at $k_\theta\rho_s = 0.1$ (upper panel) and $k_\theta\rho_s = 0.4$ (lower panel). The mode in the upper panel exhibits ballooning parity, indicating a hybrid mode, whereas the mode in the lower panel displays tearing parity and is identified as an MTM, consistent with the discussion above. Switching off $\delta B_{\|}$ fluctuations stabilizes the hybrid modes, in agreement with recent studies.

Following the linear analysis, nonlinear simulations are performed using the same resolution as in the high-collisionality case, except with 384 radial (k_x) grid points with $k_{x,\min}\rho_s = 0.038$ and 32 binormal (k_y) grid points with $k_{y,\min}\rho_s = 0.05$. These parameters lead to a domain size of $(L_x, L_y) \approx (165, 126)\rho_s$, perpendicular to the field-line. Figure 13 shows the time evolution of the electron heat flux, normalized to the gyro-Bohm value, along with the nonlinear electron heat flux spectrum as a function of $k_\theta\rho_s$ for the case including $\delta B_{\|}$ fluctuations. The saturated electron heat flux reaches $Q_e = (1.89 \pm 0.34)Q_{\mathrm{GB}}$.

These results correspond to simulations excluding the Mach flow (M) and parallel flow shear (γ_P); however, the perpendicular flow shear (γ_E) is included. When M and γ_P (full physics) are included, the electron heat flux increases to $Q_e = (4.44 \pm 1.24)Q_{\mathrm{GB}}$. A possible explanation for the increase in Q_e when M and γ_P are included requires additional analysis and is therefore left for future work. The electron heat flux can be made to decrease to $Q_e = (2.26 \pm 0.33)Q_{\mathrm{GB}}$ after reducing the electron temperature gradient by just 5%, a change within experimental uncertainties and in agreement with the measured value $Q_e^{\mathrm{exp}} = (1.5 - 2.5)Q_{\mathrm{GB}}$ from power balance studies using TRANSP. Furthermore, the ratio $Q^{A_{\|}}/Q^{\mathrm{Total}} \sim 1$ and the ion turbulent heat flux is

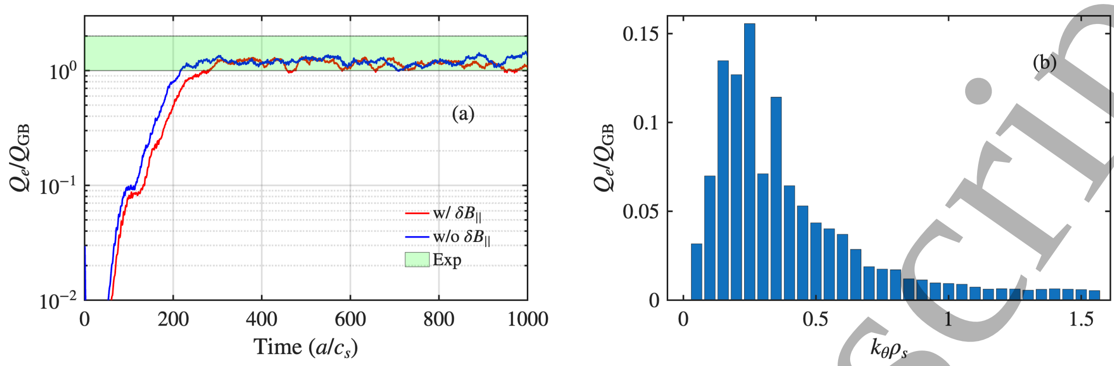

Figure 8. Nonlinear simulation results for the moderate-collisionality case. (a) Time history of the electron heat fluxes normalized with gyro-Bohm values $Q_{\rm GB}$ with the effect of $\delta B_\parallel$ fluctuations. (b) Variation of normalized electron heat flux with the normalized wavenumber $k_\theta \rho_s$.

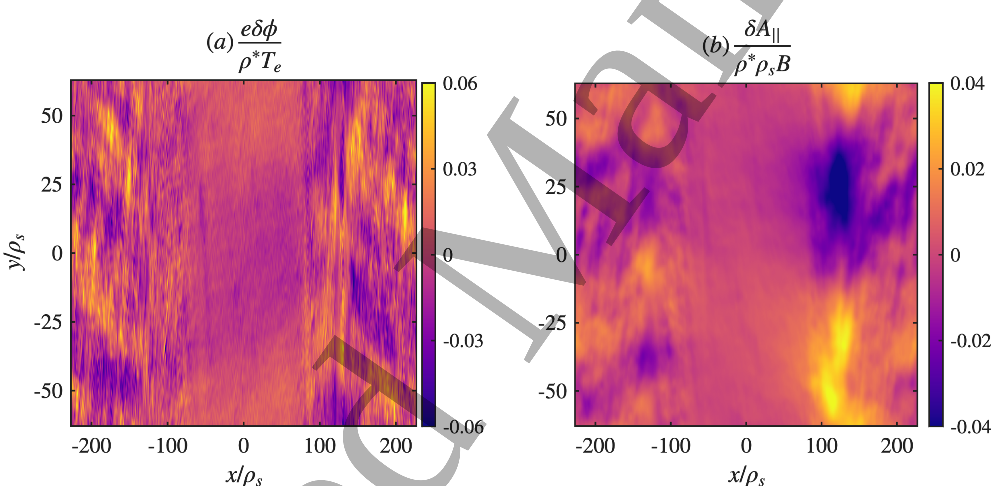

Figure 9. Contour plots of (a) $\delta\phi$ and (b) $\delta A_\parallel$ on the outer midplane at $\theta = 0$ in the nonlinear phase of the simulation for the moderate-collisionality case. Fluctuating quantities are shown without their zonal components ($k_y = 0$).

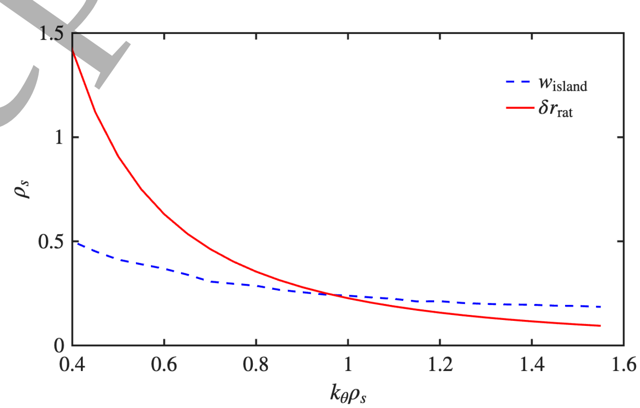

Figure 10. Estimated island width ($\mathrm{w}_{\rm island}$) and the spacing between rational surfaces ($\delta r_{\rm rat}$) from the nonlinear phase of the simulation for the moderate-collisionality case.

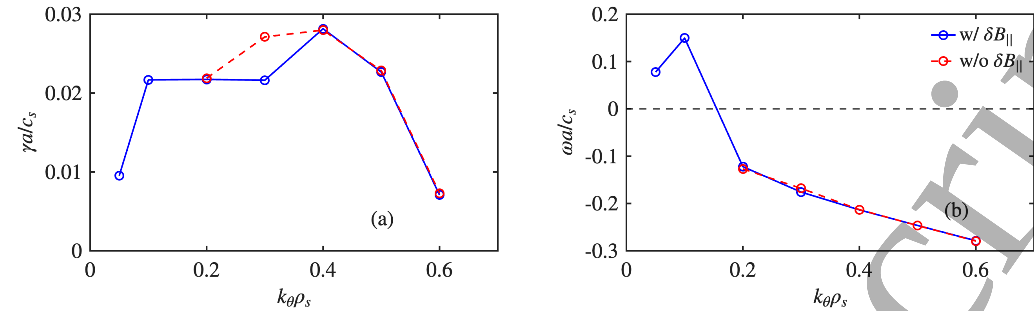

Figure 11. Linear analysis of the low-collisionality case. (a) Growth rates γ and (b) real frequencies ω versus the normalized wavenumber $k_\theta\rho_s$ with C^{6+} impurity ions included in the simulations. The effect of $\delta B_\parallel$ fluctuations on the linear spectrum is also shown.

small: $Q_i = (0.016 \pm 0.010)Q_{\rm GB}$. These results indicate that transport is entirely dominated by MTMs. The simulations (not shown here) scanning the flow shearing rate demonstrate that hybrid modes do not saturate when the flow shearing rate is smaller than their linear growth rate ($\gamma_E < \gamma_{\rm hybrid}$). One of the simulations without flow shear is discussed in Appendix D. However, under experimental conditions, the hybrid mode growth rates are approximately an order of magnitude smaller than the flow shearing rate. The strong sensitivity of turbulent fluxes across all transport channels to the flow shear, and their subsequent increase to very large values owing to the onset of hybrid twisting-parity modes, is consistent with recent findings from studies of non-NBI heated plasmas in STEP [56]. As a result, they are effectively suppressed in the nonlinear phase. On the other hand, $\vec{E}\times\vec{B}$ shear reduces MTM-driven transport as well, however, finite transport levels persist over a range of experimentally relevant flow shear values [31]. The calculations of neoclassical ion heat transport using the drift-kinetic code NEO [57] yields $Q_i^{\rm neo} \sim 0.83\,Q_{\rm GB}$, which is consistent with the the experimental value of $Q_i \sim 0.79\,Q_{\rm GB}$ calculated from power balance studies using TRANSP. Thus, the ion thermal transport remains close to neoclassical levels, consistent with NSTX experiments [24, 25]. Consequently, MTMs are the primary mechanism driving the observed electron heat flux in this low-collisionality scenario. The $\delta B_\parallel$ fluctuations have a negligible effect on transport, further confirming the suppression of hybrid modes in the nonlinear phase. The nonlinear spectrum of turbulent heat flux peaks at $k_\theta\rho_s \sim 0.2$. Extensive convergence tests confirm the robustness of these results with respect to numerical resolution (see Appendix C).

Figure 14 shows the contour plots of the perturbed fields, $\delta\phi$ and $\delta A_\parallel$, on the outer midplane ($\theta = 0$). The $\delta B_\parallel$ fluctuations are relatively much smaller than the $\delta A_\parallel$ fluctuations, in accordance with the linear analysis, and therefore are again not shown here. In particular, $\delta A_\parallel$ exhibits elongated structures spanning the full radial extent of the flux tube, similar to the high-collisionality case discussed in Sec. 2.1. Sensitivity tests with an expanded radial domain show no significant change in Q_e, confirming that the observed structures and transport are physical.

Figure 15 shows the magnetic island width, $\mathrm{w}_{\rm island}$, and the spacing between rational

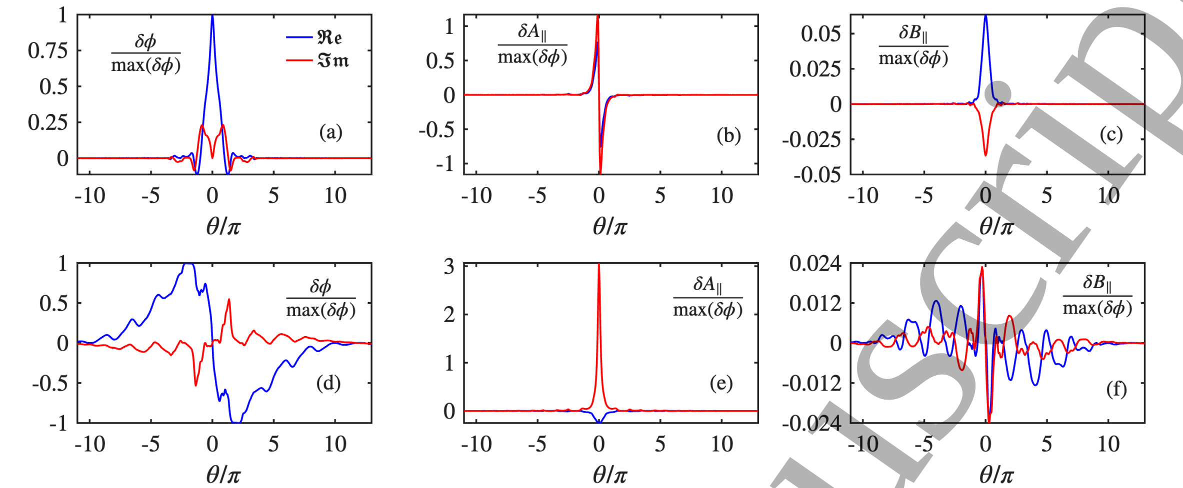

Figure 12. Eigenfunctions (a, d) $\delta\phi$, (b, e) $\delta A_\parallel$, and (c, f) $\delta B_\parallel$ as a function of the ballooning angle for $k_\theta\rho_s = 0.1$ (upper panel) and $k_\theta\rho_s = 0.4$ (lower panel) for the low-collisionality case. The values are normalized by $\max(\delta\phi)$.

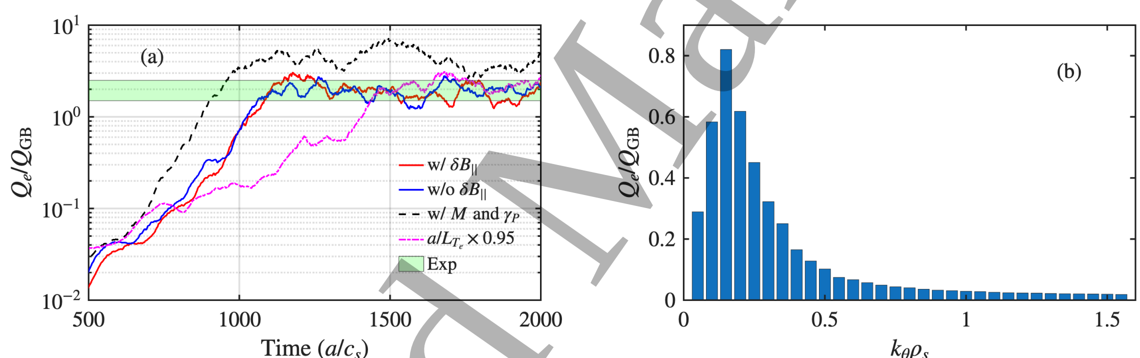

Figure 13. Nonlinear simulation results for the low-collisionality case. (a) Time history of the electron heat fluxes normalized with gyro-Bohm values $Q_{\rm GB}$ with the effect of $\delta B_\parallel$ fluctuations. (b) Variation of normalized electron heat flux with the normalized wavenumber $k_\theta\rho_s$.

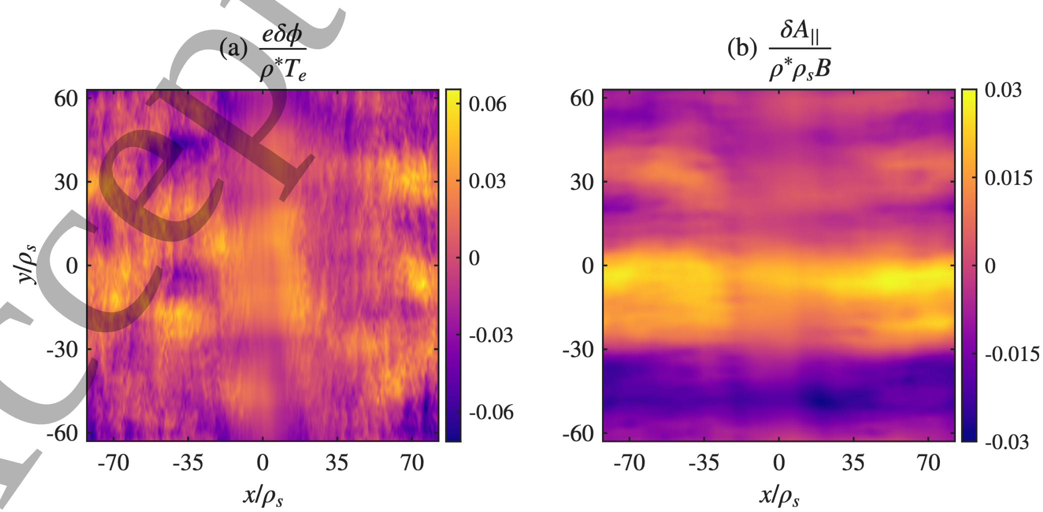

Figure 14. Contour plots of (a) $\delta\phi$ and (b) $\delta A_\parallel$ on the outer midplane at $\theta = 0$ in the nonlinear phase of the simulation for the low-collisionality case.

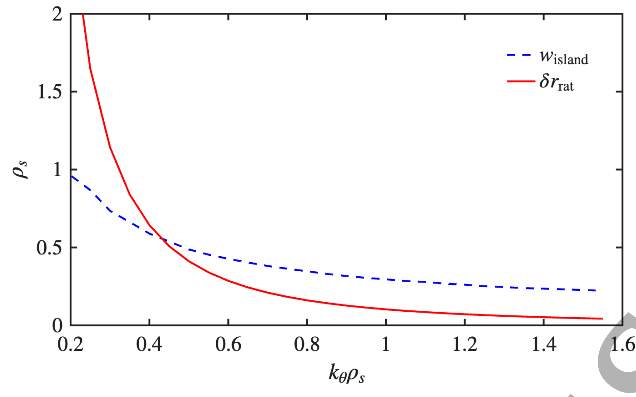

Figure 15. Estimated island width ($\mathrm{w}_{\mathrm{island}}$) and spacing between the rational surfaces (δr_{rat}) from the nonlinear phase of the simulation for the low-collisionality case.

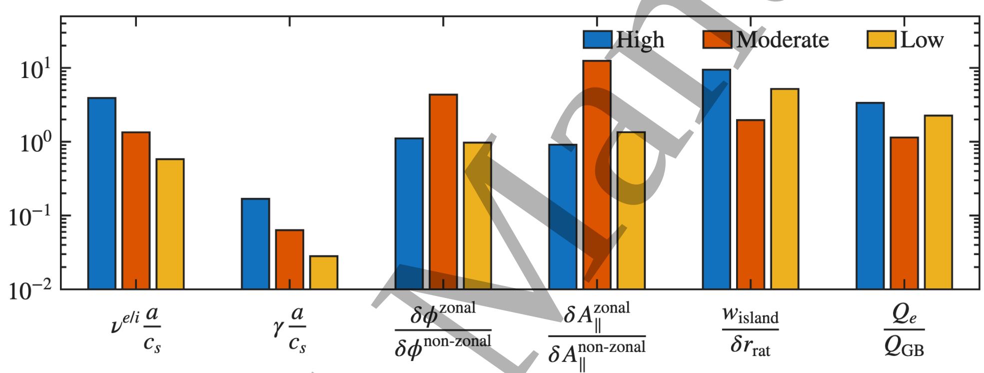

Figure 16. Summary of the results from the NSTX discharges with high-, moderate- and low-collisionality.

surfaces, estimated from the saturated phase of the nonlinear simulations, as a function of the normalized wavenumber $k_\theta \rho_s$. The island overlap criterion, $\mathrm{w}_{\mathrm{island}} > \delta r_{\mathrm{rat}}$, is satisfied for $k_\theta \rho_s > 0.43$, with the ratio $\mathrm{w}_{\mathrm{island}}/\delta r_{\mathrm{rat}}$ reaching approximately 5.18 at the highest wavenumber. This substantial overlap produces stochastic magnetic field lines, providing an effective mechanism for electron thermal transport in this low-collisionality regime.

2.4. Summary of MTM-driven transport in NSTX

Figure 16 summarizes the results of the gyrokinetic analysis for the NSTX cases. It presents the electron–ion collisionality, the linear growth rate of the most unstable MTM, the amplitudes of the zonal components of the electrostatic potential and parallel magnetic vector potential relative to the largest non-zonal mode which dominates the transport, the ratio of magnetic island width to the spacing between rational surfaces at the highest normalized wavenumber, and the electron heat flux for the high-, moderate-, and low-collisionality cases. All values are shown on a logarithmic scale, as the quantities differ by more than an order of magnitude in normalized units. The linear growth rate of the most unstable MTM follows a trend similar to that of the electron–ion collisionality, reflecting the collisional drive of MTMs. The amplitudes of the zonal components of the electrostatic potential and parallel magnetic vector potential are comparable for the high- and low-collisionality cases but are significantly larger in the moderate-collisionality case. In particular, the zonal component of the parallel magnetic vector potential in the moderate-collisionality regime is nearly an order of magnitude larger than in the other two cases. Zonal fields act as a key saturation mechanism for MTM-driven turbulence [51, 11], which is reflected in the electron heat flux trend. The moderate-collisionality case exhibits the lowest electron heat flux among the three cases. Similarly, the ratio of island width to the spacing between rational surfaces at the highest normalized wavenumber, a measure of magnetic field line stochasticity, follows a trend consistent with the electron heat flux, confirming that MTM-driven transport is mediated by stochastic field lines. This consistency between electron thermal transport and the island overlap criterion has been observed in NSTX experiments [58]. Thus, these nonlinear gyrokinetic simulations demonstrate the capability of CGYRO to self-consistently capture MTM-driven electron heat transport consistent with experimental observations, thereby providing a basis for the subsequent analysis of MTM stability and transport in NSTX-U–like plasmas. It is also important to note that the dominance of zonal flows/fields in the moderate-collisionality case and the resulting trend of electron heat flux may not arise solely from differences in collisionality, but may also be influenced by other equilibrium and profile parameters that differ appreciably among the three cases. To address this, a sensitivity analysis is presented in Sec. 2.5.

2.5. Scaling analysis and exploration of MTMs in NSTX-U–like plasmas

In NSTX-U, the collisionality is expected to be even lower than in the NSTX cases discussed earlier in this study. To qualitatively access the NSTX-U–relevant regime, we first perform linear simulations based on the NSTX high-collisionality discharge #120968 at 560 ms and $r = 0.6a$, while varying the collisionality and keeping all other parameters fixed. The simulations include two kinetic species, thermal ions and electrons, while impurity effects are retained by setting an effective charge of $Z_{\mathrm{eff}} = 2.87$.

In contrast to the Sugama collision operator used in the simulations presented earlier in this work, the results shown in this section employ the Lorentz collision operator. The Sugama collision operator is a more physically complete approximation to the gyro-averaged Fokker–Planck collision operator and describes multi-species collisions, including pitch-angle scattering, energy diffusion, and momentum- and energy-conserving restoring terms. In contrast, the Lorentz operator is a simplified pitch-angle scattering model that neglects energy diffusion and conservation-restoring terms and does not explicitly include ion-ion collisions. A comparison of these operators and their influence on various micro-instabilities has been explored in [59]. Importantly, in the context of MTMs, for which electron-ion collisions play a dominant role in mediating the tearing response, the Lorentz collision operator provides a reasonable

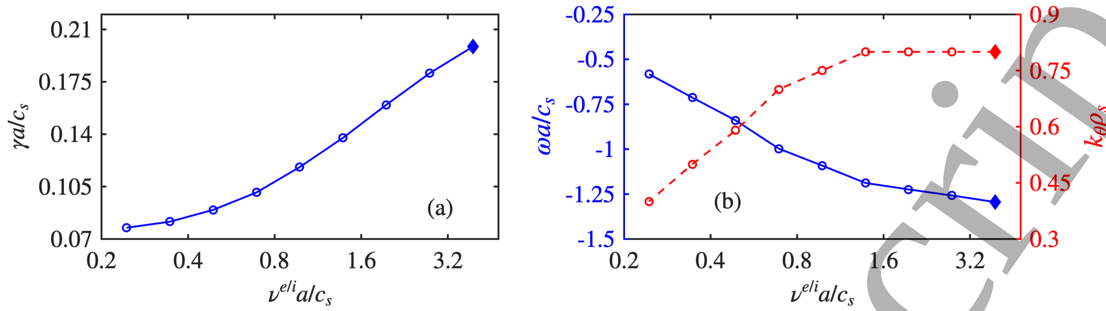

Figure 17. Linear gyrokinetic analysis showing the scaling of MTMs for high-collisionality NSTX case with collisionality. (a) Variation of the growth rate γ, and (b) frequency ω and normalized wavenumber $k_\theta \rho_s$ of the most dominant MTM with the electron-ion collisionality $\nu^{e/i}$.

approximation and has been widely employed in earlier studies [10, 22, 23, 31]. In addition, the Lorentz operator enables the use of a realistic value of $Z_{\text{eff}} = 2.87$ while retaining a reduced two-species model (thermal ions and electrons), thereby avoiding the need to explicitly include impurity species in the simulations. This choice also enables reproducing the full linear MTM spectrum with two species, although some discrepancies in growth rates and mode frequencies remain. The linear simulations use the same numerical resolution as described in Sec. 2.1.

Figure 17 shows the dependence of the growth rate, frequency, and wavenumber of the most unstable MTM on the electron–ion collisionality. As collisionality is reduced from the experimental value (denoted by a diamond symbol in this and subsequent figures) by a factor of 16, the MTM growth rate decreases by approximately a factor of 2.5, with a noticeably weaker dependence in the low-collisionality regime. This behavior suggests that, at sufficiently low-collisionality, MTMs stability may be limited by other parameters, most notably the electron temperature gradient, which provides the primary drive for MTMs. Over the same collisionality scan, the dominant MTM wavenumber shifts from $k_\theta \rho_s = 0.8$ to 0.4, while both the frequency and wavenumber exhibit a steeper variation in the low-collisionality regime.

Notably, even after an order-of-magnitude reduction in collisionality, MTMs remain the dominant instability in this high-collisionality NSTX case. This behavior contrasts with other NSTX discharges, where hybrid modes coexist with MTMs, and reduced collisionality can promote a transition toward TEMs as collisional detrapping weakens and trapped-electron drive becomes more effective. The presence of multiple competing instabilities in such cases complicates the separation of transport contributions from MTMs and other modes in the nonlinear simulations. For these reasons, the NSTX high-collisionality discharge is chosen as the baseline case for investigating the scaling of MTM-driven electron heat transport with collisionality. It is worth noting that collisionality has a destabilizing effect on MTMs in the parameter regime explored in this work, in contrast to electrostatic instabilities such as ITG modes and collisionless TEMs, for which increasing collisionality generally leads to stabilization through enhanced collisional damping and electron de-trapping mechanisms [60].

After analyzing the evolution of the linear spectrum with collisionality, nonlinear simulations are carried out using the same resolution as in the high-collisionality case discussed in Sec. 2.1, except with 576 k_x grid points with $k_{x,\min}\rho_s = 0.056$ and 32 k_y grid points with $k_{y,\min}\rho_s = 0.042$. Figure 18 shows the variation of MTM-driven electron heat flux with electron–ion collisionality on a log–log scale. The vertical lines represent error bars corresponding to the standard deviation of the fluxes, calculated from their time histories during the saturated phase of the nonlinear simulation. The experimental equilibrium flow shearing rate is included in this scaling analysis, which was not present in the previously performed scaling studies using GYRO [23]. It is important to note that the simulations at the experimental collisionality lead to $Q_e = (2.69 \pm 0.30)Q_{\rm GB}$, which is slightly lower than the electron heat flux from the nonlinear simulations discussed in Sec. 2.1 with three kinetic species. The lowest point on the x-axis represents the collisionality $\nu^{e/i} = 0.49c_s/a$, which is slightly smaller than the low-collisionality NSTX case discussed in Sec. 2.3.

Overall, within the parameter regime explored in this work, the observed MTMs exhibit characteristics of collisional MTMs, with the electron heat flux driven by MTMs decreasing as collisionality is reduced. This trend is consistent with the underlying physics of MTMs, which rely on collisional electron dissipation within a narrow reconnecting layer to facilitate magnetic reconnection. In the collisionless limit, electrons remain strongly tied to magnetic field lines through rapid parallel motion, and magnetic flux is approximately frozen, preventing changes in magnetic topology. However, finite electron collisionality introduces dissipation through electron scattering, which enhances the electron current response and thus relaxes the frozen-in constraint, enabling reconnection of perturbed magnetic field lines and the growth of tearing-parity magnetic fluctuations. Consequently, MTMs are typically destabilized at finite collisionality, while sufficiently low collisionality tends to suppress the mode by reducing the dissipation necessary to sustain reconnection. As collisionality decreases, enhanced parallel electron streaming due to weaker dissipation across the layer weakens the tearing response, reduces magnetic flutter transport, and consequently lowers the nonlinear saturation level of MTMs. For collisionalities $\nu^{e/i} \gtrsim c_s/a$, the electron heat flux exhibits a trend similar to that reported in previous studies [23], with $\chi_e^\star \sim \nu_\star$, where the electron heat transport coefficient $\chi_e = -\frac{Q_e}{n_e \nabla T_e}$ is normalized by the gyro-Bohm value $\chi_{\rm GB} = \rho_s^2 c_s/a$ (i.e., $\chi_e = \chi_e^\star \chi_{\rm GB}$) and $\nu_\star = \nu^{e/i} a/c_s$. However, for $\nu^{e/i} \lesssim c_s/a$, the electron heat flux decreases more steeply, following a much stronger scaling, $\chi_e^\star \sim \nu_\star^4$. Consequently, around $\nu^{e/i} \approx c_s/a$, two distinct scaling regimes of MTM-driven electron heat flux with collisionality are observed. Further analysis is performed to explore this transition in the electron heat flux with collisionality.

Figure 19 shows the variation of the zonal components of the electrostatic potential and the parallel magnetic vector potential, each normalized to their corresponding largest non-zonal modes that dominate transport, as a function of electron–ion collisionality. Both ratios increase with decreasing collisionality. The zonal component of the electrostatic potential relative to the largest non-zonal mode increases by a factor

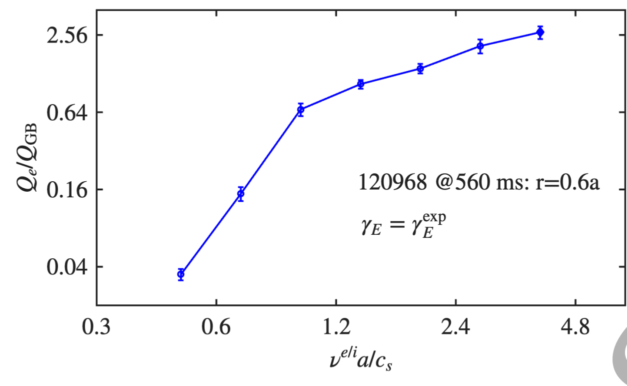

Figure 18. Variation of the electron heat flux normalized with the gyro-Bohm value $Q_{\rm GB}$ with the electron-ion collisionality $\nu^{e/i}$.

of ~ 2.5 as the collisionality is reduced from $\nu^{e/i} = 3.91c_s/a$ to $0.49c_s/a$, whereas the zonal component of the parallel magnetic vector potential grows by nearly an order of magnitude over the same range.

Notably, the trend of $\delta A_\parallel^{\rm zonal}/\delta A_\parallel^{\rm non\text{-}zonal}$ closely follows that of the electron heat flux shown in Fig. 18, highlighting the important role of zonal fields in the nonlinear saturation of MTM-driven turbulence, consistent with previous studies [51, 11]. Consequently, stronger zonal fields lead to a reduction in MTM-driven turbulence and the associated electron heat flux. Reducing the collisionality below $\nu^{e/i} = 0.49c_s/a$ results in the complete suppression of nonlinear turbulence and the associated transport by the zonal fields.

It is important to note that, in the present analysis, no unstable ETG modes are found that could otherwise contribute to electron thermal transport. This may influence the scaling of electron thermal transport with collisionality, particularly in the low-collisionality regime where MTM-driven transport becomes negligible. A detailed exploration of the collisionality scaling of ETG linear stability, as well as the resulting nonlinear turbulence and transport in NSTX and NSTX-U, is therefore left for future work. In fact, multiscale simulations might be necessary when both MTMs and ETGs are unstable [61].

The scaling of electron heat flux with collisionality has been studied for ETG turbulence in MAST using electrostatic local nonlinear gyrokinetic simulations with adiabatic ions [27], where a reduction in electron heat transport due to enhanced zonal flows was observed at low collisionality. The resulting scaling was found to be qualitatively consistent with the experimentally observed scaling of the energy confinement time [21]. In addition, the collisional damping of zonal flows excited by ITG turbulence has also been investigated in conventional tokamaks using electrostatic global nonlinear gyrokinetic simulations [62].

The role of zonal flows/fields in regulating turbulence depends critically on their relative intensity: stronger zonal flows/fields are more effective at regulating plasma turbulence. The intensity of the zonal flows/fields is determined by the competition

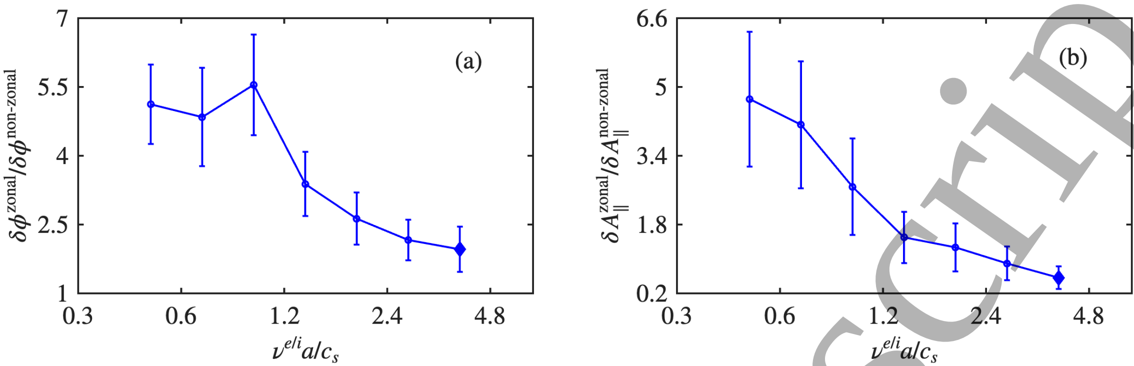

Figure 19. Variation of the zonal component of electrostatic potential (a) and the parallel magnetic vector potential (b) relative to the largest non-zonal mode with the electron-ion collisionality $\nu^{e/i}$.

between their generation and damping mechanisms. Since zonal flows/fields are nonlinearly generated by the turbulence itself, stronger turbulence generally leads to stronger zonal flows/fields. On the other hand, collisions can lead to their damping. The collisions damp zonal structures associated with flows/fields through dissipating the velocity perturbations and currents associated with the parallel electron flow. In particular, increased collisionality enhances viscous damping of zonal flows and resistive damping of the parallel currents associated with zonal fields, reducing the amplitude and persistence of zonal structures and thereby weakening their nonlinear regulation of MTM turbulence. However, the relative importance of these mechanisms is expected to vary across parameter regimes and is not quantified in the present work.

It is important to note that, for the NSTX cases analyzed, the electron heat fluxes do not differ dramatically, with a maximum variation of about a factor of three. In contrast, the collisionality scaling for the high-collisionality case exhibits a variation in electron heat flux by a factor of approximately 75 over a collisionality range comparable to that separating the high- and low-collisionality NSTX cases. This suggests that other equilibrium and profile parameters, which differ substantially among the three discharges, also play a critical role in limiting the linear MTM stability, zonal flows/fields and the resulting electron heat transport. In addition, collisionality and electron temperature gradient are observed to be coupled in NSTX [7]. Therefore, building on the collisionality scan presented above, we perform a sensitivity analysis of various equilibrium and profile parameters to further examine trends in MTM-driven transport relevant to NSTX-U conditions. Due to the complex landscape of instabilities in STs, the following analysis is restricted to modest variations in equilibrium and profile parameters; larger deviations can excite additional instabilities [22].

We first investigate the sensitivity of the electron heat flux to the equilibrium flow shear. Figure 20 shows the variation of the MTM-driven electron heat flux as a function of the equilibrium flow shear, which is varied by ±50% around the experimental value of the baseline case. This sensitivity is examined at both the high- and low-collisionality, $\nu^{e/i} = 3.91c_s/a$ and $\nu^{e/i} = 0.49c_s/a$, respectively. At high-collisionality, the electron

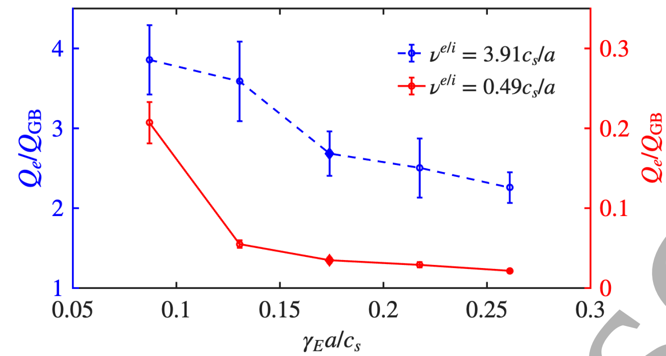

Figure 20. Variation of the electron heat flux normalized with the gyro-Bohm value $Q_{\rm GB}$ with the flow shearing rate γ_E for the electron-ion collisionality $\nu^{e/i} = 3.91c_s/a$ and $\nu^{e/i} = 0.49c_s/a$.

heat flux changes by a factor of ~ 2, whereas at the low-collisionality it varies by nearly an order of magnitude, indicating a much stronger sensitivity to equilibrium flow shear at low collisionality.

We next explore the sensitivity of the electron heat flux to the density gradient and the electron β. Figure 21 shows the variation of the MTM-driven electron heat flux with the electron density gradient and electron β for the collisionalities $\nu^{e/i} = 3.91c_s/a$ and $\nu^{e/i} = 0.49c_s/a$. The parameters are varied by $\pm 20\%$ around the experimental values of the baseline high-collisionality case; larger deviations lead to a transition to other instabilities.

An increase in the density gradient towards positive values results in a destabilization of MTMs. These results align with the previous findings in NSTX [22] and MAST [16, 20]. In a similar manner, increasing the electron β further destabilizes MTMs. Both the electron and ion density gradients are varied simultaneously to maintain quasi-neutrality. At high collisionality ($\nu^{e/i} = 3.91c_s/a$), varying density gradient and electron β leads to a variation in the electron heat flux by approximately two- and three-folds, respectively. At low collisionality ($\nu^{e/i} = 0.49c_s/a$), MTMs become linearly stable when both the electron density gradient and electron β are reduced below their experimental values. In contrast, increasing these parameters leads to increase in electron heat flux by about an order of magnitude.

The electron temperature gradient is the primary drive for MTMs. Figure 22 shows the variation of the MTM-driven electron heat flux with the electron temperature gradient at low-collisionality ($\nu^{e/i} = 0.49c_s/a$). At low-collisionality, increasing the electron temperature gradient by 20% relative to the baseline enhances the electron heat flux by a factor of ~ 30 due to the stronger linear drive, whereas reducing the gradient by 20% stabilizes the MTMs. At high-collisionality ($\nu^{e/i} = 3.91c_s/a$), reducing the electron temperature gradient below the baseline value significantly reduces the linear drive resulting in negligible electron heat flux, whereas increasing the electron temperature gradient beyond the baseline value triggers ETG modes in addition to MTMs. Recent CGYRO simulations for NSTX indicate a significant reduction in MTM

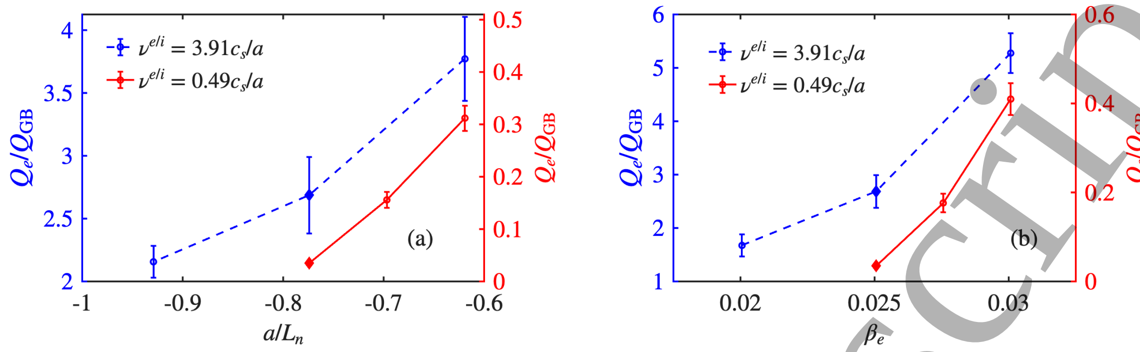

Figure 21. Variation of the electron heat flux normalized with the gyro-Bohm value $Q_{\rm GB}$ with the normalized plasma density a/L_n (a) and the electron β (b) for the electron-ion collisionality $\nu^{e/i} = 3.91c_s/a$ and $\nu^{e/i} = 0.49c_s/a$.

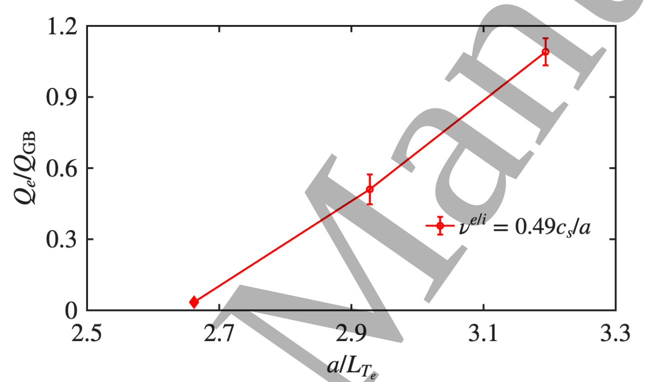

Figure 22. Variation of the electron heat flux normalized with the gyro-Bohm value $Q_{\rm GB}$ with the normalized electron temperature gradient a/L_{T_e} for the electron-ion collisionality $\nu^{e/i} = 0.49c_s/a$.

turbulence at multi-scale resolution, even when ETG turbulence is weak [61], suggesting that accurate predictions of electron heat flux require multi-scale simulations.

In addition to plasma parameters such as collisionality, the electron temperature gradient, density gradient, electron β, and equilibrium flow shear, the linear stability of MTMs and the corresponding nonlinear transport are also sensitive to equilibrium parameters, namely the safety factor q and the magnetic shear $\hat{s}$. We, therefore, explore the sensitivity of the MTM-driven electron heat flux to 20% variations in q and $\hat{s}$. Figure 23 shows the electron heat flux as a function of q and $\hat{s}$ for the collisionality cases $\nu^{e/i} = 3.91c_s/a$ and $0.49c_s/a$.

Numerous investigations have explored the complex dependence of MTM linear stability and nonlinear transport on q and $\hat{s}$ [22, 17, 20]. Varying q has little effect on the linear stability of MTMs; however, nonlinear simulations reveal a significant change in the electron heat flux (by factors of $\sim$ 15 and 45 at high and low collisionalities, respectively) due to a 2–3-fold variation in the amplitude of the zonal component of the parallel magnetic vector potential relative to the non-zonal mode dominating transport (Fig. 23a). The weak linear dependence of MTM instability on q suggests that moderate variations in q do not substantially alter the dominant linear drive mechanisms, which are primarily governed by electron temperature gradients, collisional electron dynamics, and magnetic drifts. However, nonlinear transport exhibits a stronger sensitivity to q, indicating that saturation physics is more strongly modified. In particular, q affects field-line connection length ($L_{||} \sim qR$), which modify the nonlinear coupling to zonal fields. Since zonal fields regulate MTM turbulence through shearing and modification of parallel electron dynamics, changes in q can significantly alter the amplitude and efficacy of these zonal structures, leading to a stronger nonlinear dependence.

Similarly, for $\nu^{e/i} = 3.91c_s/a$, reducing $\hat{s}$ does not modify the linear growth rate, yet the electron heat flux increases nonlinearly by a factor of ~ 3 (Fig. 23b). This increase is attributed to enhanced magnetic island widths, both due to a decrease in $\hat{s}$ (see Eq. 2) and an increase in $\delta B/B$ fluctuations in the nonlinear saturation, which lead to increased field-line stochasticity, even though the spacing between rational surfaces increases too. At low-collisionality, $\nu^{e/i} = 0.49c_s/a$, decreasing $\hat{s}$ not only increases the magnetic island width but also raises the linear growth rate by $\sim 40\%$, resulting in a pronounced increase in electron heat transport by a factor of ~ 30. In these cases, the amplitude of the zonal component of $\delta A_{||}$ remains relatively less sensitive to variations in $\hat{s}$.

Therefore, magnetic shear affects MTMs in a complex way, and it generally enters through the magnetic shear length, $L_s = Rq/\hat{s}$, and influences the parallel connection length, tearing-layer structure, and mode coupling. Consequently, $\hat{s}$ can affect the linear MTM growth rate by modifying the tearing-layer physics and parallel electron dynamics. The above results further indicate that the sensitivity of MTMs to $\hat{s}$ depends on collisionality. At high collisionality, the MTM drive is dominated by collisional electron dissipation within the reconnecting layer, making the instability relatively insensitive to moderate variations in magnetic shear. In contrast, at low collisionality, where the tearing response is weaker and parallel electron dynamics play a more prominent role, variations in $\hat{s}$ have a stronger influence on mode structure and coupling, resulting in a more pronounced dependence of the MTM growth rate on $\hat{s}$. A reduction in $\hat{s}$ increases L_s, allowing more radially extended mode structures and modifying the nonlinear saturation process. In the nonlinear simulations, changes in magnetic shear can also affect the fluctuation amplitude $\delta B/B$, thereby altering magnetic island widths and the degree of field-line stochasticity. The previous studies in conceptual power-plant conditions have also reported a destabilizing effect of higher q and lower $\hat{s}$ on MTMs. [20].

Based on the above discussion, in addition to collisionality, the safety factor also plays an important role in limiting zonal flows/fields. In the safety factor scan discussed above, a decrease in the safety factor leads to a reduction in electron heat transport due to enhanced zonal flows/fields. This behavior is consistent with the NSTX cases analyzed in this study, where the moderate-collisionality scenario has lower q value compared to the both high- and low-collisionality NSTX cases and, consequently, exhibits stronger zonal flows/fields. This dependence of the zonal amplitude on q is qualitatively consistent with the Rosenbluth–Hinton residual level [63].

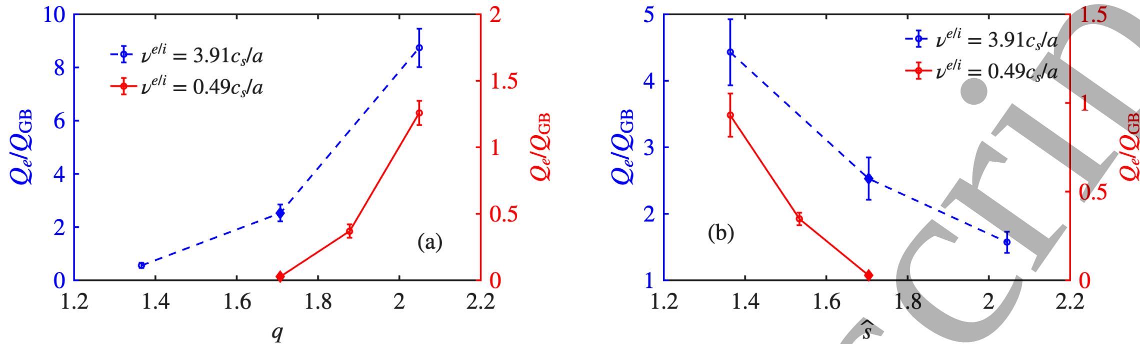

Figure 23. Variation of the electron heat flux normalized with the gyro-Bohm value $Q_{\rm GB}$ with the safety factor q (a) and the magetic shear $\hat{s}$ (b) for the electron-ion collisionality $\nu^{e/i} = 3.91c_s/a$ and $\nu^{e/i} = 0.49c_s/a$.

In principle, one could start from the high-collisionality NSTX case and systematically vary plasma parameters to transition toward the low-collisionality NSTX case, to understand the interplay of these parameters on linear MTM stability, amplitude of zonal flows/fields, and the nonlinear transport. However, a comprehensive investigation of this parametric dependence of MTM-driven electron heat flux on multiple plasma parameters is beyond the scope of the present work and is left for future studies.

Finally, in the context of the role of MTMs in the NSTX-U–relevant regime, although the low collisionality suggests that MTMs may not pose a critical limitation on overall plasma confinement, the strong sensitivity of MTM linear stability and the associated electron heat transport to various plasma parameters at low collisionality indicates that their contribution cannot be ruled out. These findings provide substantial insights into the behavior of MTMs in spherical tokamaks based on first-principles simulations and help clarify the potential role of MTM-driven electron thermal transport in future devices such as NSTX-U.

3. Conclusions and discussion

A comprehensive gyrokinetic analysis of NSTX discharges spanning high-, moderate-, and low-collisionality regimes is presented using the fully electromagnetic code CGYRO. At the radial locations considered for the discussed cases, MTMs emerge as the dominant instabilities responsible for electron thermal transport, where ETG modes are stable. The nonlinear MTM simulations reproduce experimental electron heat fluxes with significantly improved fidelity compared to previous studies. Analysis of the high-collisionality case reveals the critical importance of including impurity species to reproduce experimentally observed flux levels. In the moderate-collisionality case, enhanced zonal flows and fields play a crucial role in reducing turbulence intensity and the associated transport. At low-collisionality, the linear spectrum reveals the coexistence of MTMs and hybrid modes. These hybrid modes are characteristics of

NSTX plasmas owing to their strong shaping and enhanced electromagnetic effects at high-β. However, the equilibrium $\vec{E} \times \vec{B}$ shearing rate substantially exceeds the growth rates of hybrid modes, suppressing the associated transport and leaving ion heat fluxes near neoclassical levels, in agreement with NSTX experiments. The strong sensitivity of turbulent fluxes across all transport channels to the flow shear, and their subsequent increase to very large values owing to the onset of hybrid twisting-parity modes, is consistent with recent findings from studies of non-NBI heated plasmas in STEP [56]. Furthermore, scaling studies are performed to qualitatively assess the role of MTMs in driving electron thermal transport under NSTX-U–relevant conditions. A collisionality scan of the high-collisionality NSTX case reveals a transition to a low-collisionality regime in which enhanced zonal flows and fields limit electron thermal transport. Sensitivity studies of MTM-driven electron heat transport with respect to equilibrium flow shear, electron temperature gradient, electron β, density gradient, safety factor, and magnetic shear indicate that, even at the low collisionalities anticipated for NSTX-U, MTMs, while not expected to pose a critical limitation, are likely to remain an important contributor to electron thermal transport. These results provide a more complete understanding of MTM-driven turbulence in spherical tokamaks and guide transport predictions in NSTX-U regimes.

Acknowledgements

This work is supported by the U.S. DOE under Award Numbers DE-SC0021385 and DE-SC0013977. This research has used the resources of the NERSC, a DOE Office of Science User Facility supported by the Office of Science of the U.S. DOE under Contract No. DE-AC02-05CH11231 using NERSC award FES-ERCAP0031122. This research also used resources of the Oak Ridge Leadership Computing Facility at the ORNL, which is supported by the Office of Science of the U.S. DOE under Contract No. DE-AC05-00OR22725. The authors are grateful to Bhavin Patel and Arkaprava Bokshi for helpful discussions, and to Jeff Candy, Emily Belli and Jack Berkery for valuable comments.

Appendix A. Convergence studies for high-collisionality case

This section explores the convergence studies for the nonlinear simulations performed for the high-collisionality case discussed in Sec. 2.1. Figure A1 shows the variation of the electron heat transport driven by MTMs for different pitch angle grid points $n_\xi = 16$, maximum normalized binormal wavenumber $k_{y,\max}\rho_s$ and radial domain sizes L_x with respect to the reference case. The pitch angle grid points n_ξ is increased to 20 with respect to the reference case which uses $n_\xi = 16$. The maximum of the normalized binormal wavenumber $k_{y,\max}\rho_s$ is doubled and the radial domain size L_x is halved with respect to the reference case. These variations produce electron heat fluxes almost similar to the reference case, illustrating the robustness of results.

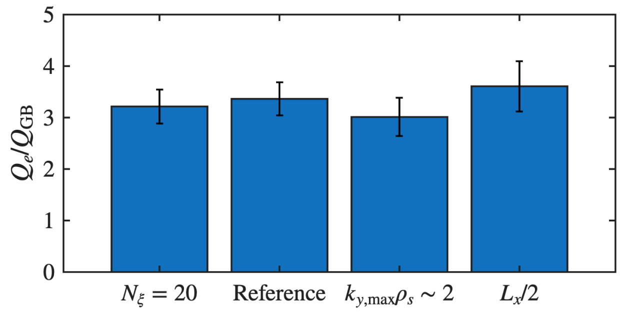

Figure A1. Variation of the electron heat flux normalized with the gyro-Bohm value $Q_{\rm GB}$ for different nonlinear simulations performed for the high-collisionality case.

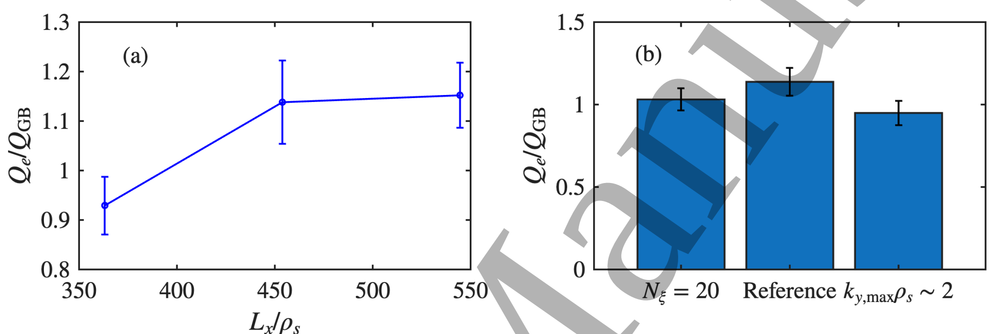

Figure B1. Variation of the electron heat flux normalized with the gyro-Bohm value $Q_{\rm GB}$ with (a) normalized radial domain size L_x/ρ_s and (b) for different nonlinear simulations performed for the moderate-collisionality case.

Appendix B. Convergence studies for moderate-collisionality case

In this section, we discuss the convergence studies for the nonlinear simulations performed for the moderate-collisionality case discussed in Sec. 2.2. Figure B1 shows the variation of the electron heat transport driven by MTMs for different radial domain sizes (a) and for different pitch angle grid points n_ξ and maximum normalized binormal wavenumber $k_{y,\max}\rho_s$ with respect to the reference case (b). The radial domain size of $L_x \approx 454\rho_s$ is good enough for the nonlinear simulations. Varying n_ξ from 16 (reference case) to 20 and $k_{y,\max}\rho_s$ from ~ 1.5 (reference case) to ~ 2 produce almost similar results. These tests indicate that the results presented in Sec. 2.2 are not affected by the change in numerical resolution.

Appendix C. Convergence studies for low-collisionality case

In this section, we discuss the convergence studies for the nonlinear simulations performed for the low-collisionality case discussed in Sec. 2.3. Figure C1 shows the variation of the electron heat transport driven by MTMs for different radial domain sizes (a) and for different pitch angle grid points and maximum normalized binormal wavenumber with respect to the reference case (b). The radial domain size of $L_x \approx 165\rho_s$ give converged results. Similarly, changing n_ξ from 16 (reference case) to 20 and $k_{y,\max}\rho_s$

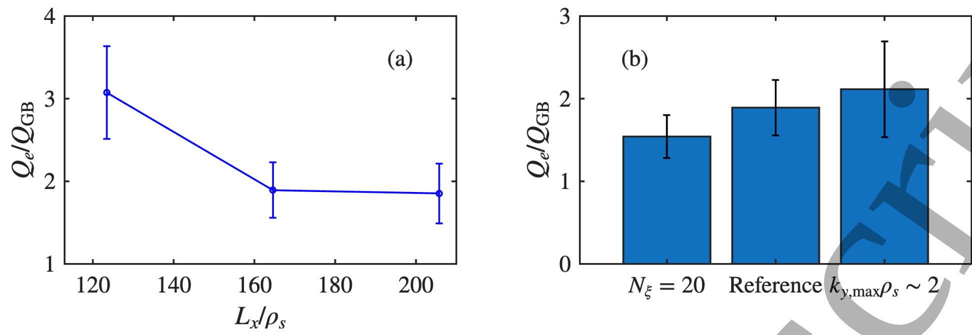

Figure C1. Variation of the electron heat flux normalized with the gyro-Bohm value $Q_{\rm GB}$ with (a) normalized radial domain size L_x/ρ_s and (b) for different nonlinear simulations performed for the low-collisionality case.

from ~ 1.5 to ~ 2 does not produce a significant change in the electron heat flux. Here, the convergence tests are shown for the cases with $M = 0$ and $\gamma_P = 0$, however, they remain valid for the case with full physics. For example, the electron heat transport for the case with $n_\xi = 20$ and experimental values of M, γ_P, is $Q_e = (3.74 \pm 0.89)Q_{\rm GB}$, which is similar to the reference case discussed in Sec. 2.3. These convergence studies indicate the robustness of simulation results with respect to the numerical resolution.

Appendix D. Nonlinear simulation of low-collisionality case without flow shear

Following the discussion of the low-collisionality NSTX case in Sec. 2.3, we now examine nonlinear simulations of the same case without flow shear while retaining the $\delta B_\parallel$ fluctuations. Figure D1 shows the time evolution of the turbulent electron and ion heat fluxes, together with their binormal spectra at two representative times during the simulation. At $t \sim 350a/c_s$, the turbulence reaches a temporary saturated state associated with the saturation of the MTM-driven turbulence. The corresponding binormal spectrum exhibits a characteristic electron heat flux spectrum dominated by MTMs. At this stage, the ion heat flux remains negligible compared to the electron heat flux and is therefore not shown. However, the low-wavenumber hybrid modes continue to grow slowly throughout the simulation. In the later stages, transport becomes predominantly carried by these hybrid modes, with $Q_i \gg Q_e$ and $\Gamma_i \gg \Gamma_e$, where Γ denotes the particle flux. These modes do not exhibit clear saturation. It is important to note that continuing the simulations further becomes computationally prohibitive because of the increasingly small time step required. Nevertheless, continuing the simulations does not alter the overall conclusions. Figure D2 shows contour plots of the electrostatic potential and parallel magnetic vector potential at $t \sim 470a/c_s$. Radially elongated structures are observed, leading to the unsaturated transport reaching extremely large values ($> 10^2 Q_{\rm GB}$) over the simulated time. These structures persist even when the radial domain size is increased. The observed behavior shares similarities with the hybrid-KBMs reported in STEP [56], which were also found to

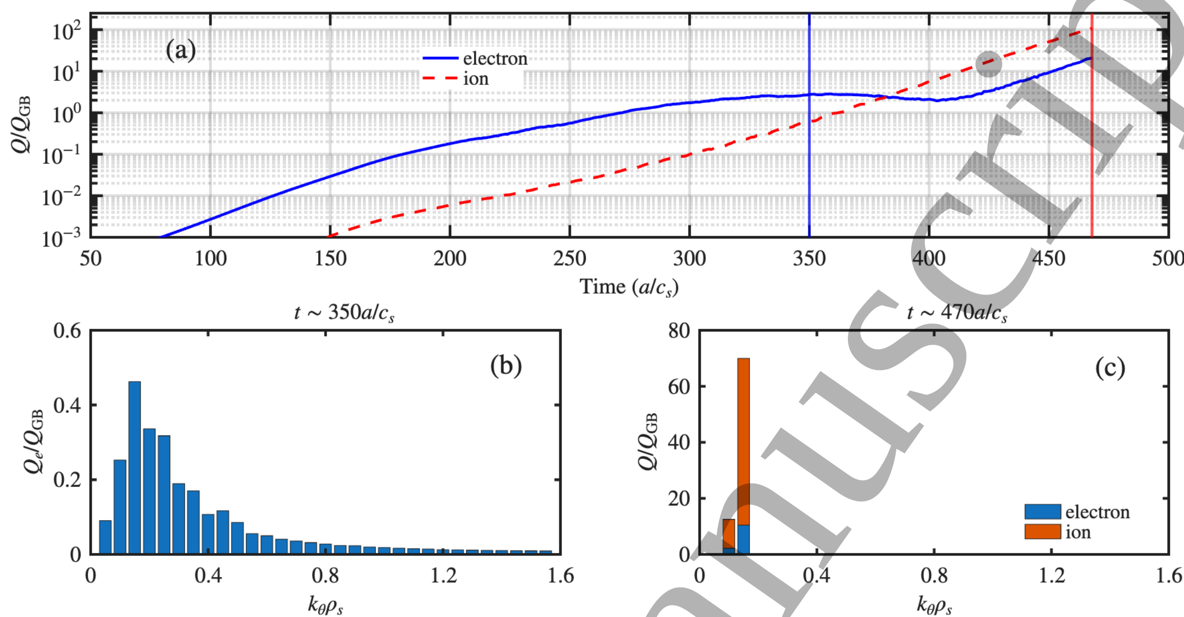

Figure D1. (a) Time history of the electron and ion heat flux normalized with the gyro-Bohm value $Q_{\rm GB}$ for the nonlinear simulation performed for the low-collisionality case without flow shear. (b) Variation of norlamized electron heat flux with normalized binormal wavenumber at $t \sim 350a/c_s$, and (c) Variation of normalized electron and ion heat flux with the normalized wavenumber at $t \sim 470a/c_s$.

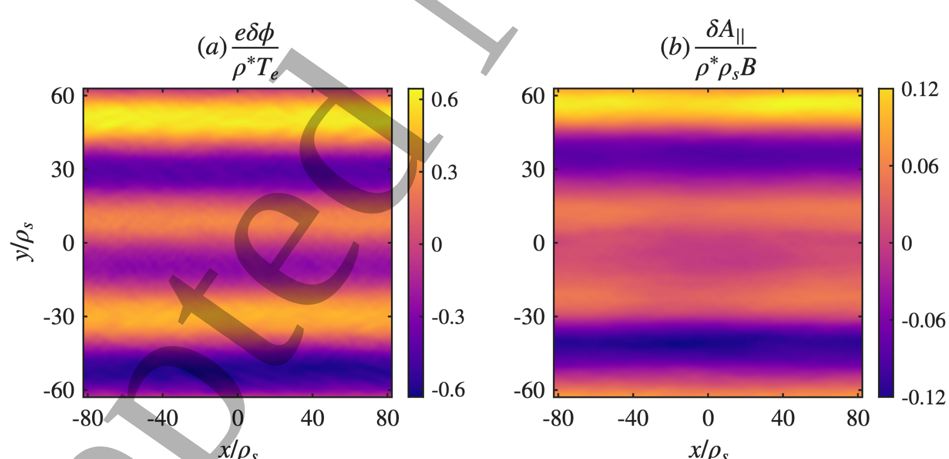

Figure D2. Contour plots of (a) $\delta\phi$ and (b) $\delta A_{\|}$ on the outer midplane at $\theta = 0$ in the nonlinear phase of the simulation at $t \sim 470a/c_s$ for the low-collisionality case without flow shear.

produce states of extremely high transport in the absence of flow shear. These results are particularly important for the design of ST reactor concepts, which may have to operate without an NBI momentum source.

References

[1] D. Kingham, M. Gryaznevich, "The spherical tokamak path to fusion power: Opportunities and challenges for development via public–private partnerships", Phys. Plasmas, **13**, 042507 (2024).

[2] W. Horton, "Drift waves and transport", Rev. Mod. Phys. **71**, 35 (1999).

[3] S.M. Kaye, J.W. Connor and C.M. Roach, "Thermal confinement and transport in spherical tokamaks: a review", Plasma Phys. Control. Fusion **63**, 123001 (2021).

[4] A.E. Costley, S.A.M. McNamara, "Fusion performance of spherical and conventional tokamaks: implications for compact pilot plants and reactors", Plasma Phys. Control. Fusion **63**, 035005 (2021).

[5] S. Moradi, I. Pusztai, W. Guttenfelder, T. Fülöp and A. Mollén, "Microtearing modes in spherical and conventional tokamaks", Nucl. Fusion **53**, 063025 (2013).

[6] M. Ono et. al., "Exploration of spherical torus physics in the NSTX device", Nucl. Fusion **40**, 557 (2000).

[7] S. Kaye, S. Gerhardt, W. Guttenfelder, R. Maingi, R. Bell, A. Diallo, B. LeBlanc, and M. Podesta, "The dependence of H-mode energy confinement and transport on collisionality in NSTX", Nucl. Fusion **53**, 063005 (2013).

[8] S.M. Kaye, W. Guttenfelder, R.E. Bell, S.P. Gerhardt, B.P. LeBlanc, R. Maingi, "Reduced model prediction of electron temperature profiles in microtearing-dominated National Spherical Torus eXperiment plasmas", Phys. Plasmas **21**, 082510 (2014).

[9] J.F. Drake, N.T. Gladd, C.S. Liu, and C.L. Chang, "Microtearing modes and anomalous transport in tokamaks," Phys. Rev. Lett. **44**, 994–997 (1980).

[10] W. Guttenfelder, J. Candy, S.M. Kaye, W.M. Nevins, E. Wang, R.E. Bell, G.W. Hammett, B.P. LeBlanc, D.R. Mikkelsen and H. Yuh, "Electromagnetic Transport from Microtearing Mode Turbulence", Phys. Rev. Lett. **106**, 155004 (2011).

[11] M. Giacomin, D. Dickinson, D. Kennedy, B.S. Patel and C.M. Roach, "Nonlinear microtearing modes in MAST and their stochastic layer formation", Plasma Phys. Control. Fusion **65**, 095019 (2023).

[12] D. Kennedy, M. Giacomin, F.J. Casson, D. Dickinson, W.A. Hornsby, B.S. Patel and C.M. Roach, "Electromagnetic gyrokinetic instabilities in STEP", Nucl. Fusion **63**, 126061 (2023).

[13] W. Guttenfelder et. al., "Progress in simulating turbulent electron thermal transport in NSTX", Nucl. Fusion **53**, 093022 (2013).

[14] Y. Ren, E. Belova, N. Gorelenkov, W. Guttenfelder, S.M. Kaye, E. Mazzucato, J.L. Peterson, D.R. Smith, D. Stutman, K. Tritz, W.X. Wang, H. Yuh, R.E. Bell, C.W. Domier and B.P. LeBlanc, "Recent progress in understanding electron thermal transport in NSTX", Nucl. Fusion **57**, 072002 (2017).

[15] D.J. Applegate, C.M. Roach, J.W. Connor, S.C. Cowley, W. Dorland, R.J. Hastie, and N. Joiner, "Micro-tearing modes in the Mega Ampere Spherical Tokamak", Plasma Phys. Control. Fusion **49**, 1113 (2007).

[16] D. Dickinson1, C.M. Roach, S. Saarelma, R. Scannell, A. Kirk, and H.R. Wilson, "Kinetic Instabilities that Limit β in the Edge of a Tokamak Plasma: A Picture of an H-Mode Pedestal", Phys. Rev. Lett. **108**, 135004 (2012).

[17] D. Dickinson, C.M. Roach, S. Saarelma, R. Scannell, A. Kirk and H.R. Wilson, "Microtearing modes at the top of the pedestal", Plasma Phys. Control. Fusion **55**, 074006 (2013).

[18] M. Kotschenreuther, W. Dorland, Q.P. Liu, M.C. Zarnstorff, R.L. Miller and Y.R. Lin-Liu, "Attaining neoclassical transport in ignited tokamaks", Nucl. Fusion **40**, 677 (2000).

[19] H.R. Wilson et al., "Integrated plasma physics modelling for the Culham steady state spherical tokamak fusion power plant", Nucl. Fusion **44**, 917 (2004).

[20] B.S. Patel, D. Dickinson, C.M. Roach, and H.R. Wilson, "Linear gyrokinetic stability of a high non-inductive spherical tokamak", Nucl. Fusion **62**, 016009 (2022).

[21] M. Valovič et al., "Collisionality and safety factor scalings of H-mode energy transport in the

MAST spherical tokamak", Nucl. Fusion **51**, 073045 (2011).

[22] W. Guttenfelder, J. Candy, S.M. Kaye, W.M. Nevins, R.E. Bell, G.W. Hammett, B.P. LeBlanc, H. Yuh, "Scaling of linear microtearing stability for a high collisionality National Spherical Torus Experiment discharge", Phys. Plasmas **19**, 022506 (2012).

[23] W. Guttenfelder, J. Candy, S.M. Kaye, W.M. Nevins, E. Wang, J. Zhang, R.E. Bell, N.A. Crocker, G.W. Hammett, B.P. LeBlanc, D.R. Mikkelsen, Y. Ren, H. Yuh, "Simulation of microtearing turbulence in national spherical torus experiment", Phys. Plasmas **19**, 056119 (2012).

[24] S.M. Kaye, R.E. Bell, D. Gates, B.P. LeBlanc, F.M. Levinton, J.E. Menard, D. Mueller, G. Rewoldt, S.A. Sabbagh, W. Wang, and H. Yuh, "Scaling of Electron and Ion Transport in the High-Power Spherical Torus NSTX", Phys. Rev. Lett. **98**, 175002 (2007).

[25] S. Kaye, F. Levinton, D. Stutman, K. Tritz, H. Yuh, M. Bell, R. Bell, C. Domier, D. Gates, W. Horton, J. Kim, B. LeBlanc, N. Luhmann, R. Maingi, E. Mazzucato, J. Menard, D. Mikkelsen, D. Mueller, H. Park, G. Rewoldt, S. Sabbagh, D. Smith, and W. Wang, "Confinement and local transport in the National Spherical Torus Experiment (NSTX)", Nucl. Fusion **47**, 499 (2007).

[26] M. Valovič et al., "Scaling of H-mode energy confinement with Ip and BT in the MAST spherical tokamak", Nucl. Fusion **49**, 075016 (2009).

[27] G.J. Colyer, A.A. Schekochihin, F.I. Parra, C.M. Roach, M.A. Barnes, Y-c Ghim and W. Dorland, "Collisionality scaling of the electron heat flux in ETG turbulence", Plasma Phys. Control. Fusion **59**, 055002 (2017).

[28] S. Munaretto et. al., "Spherical tokamak physics research in preparation for the operation of NSTX-U", Nucl. Fusion **66**, 035001 (2026).

[29] Y. Ren, W.X. Wang, W. Guttenfelder, S.M. Kaye, J. Ruiz-Ruiz, S. Ethier, R. Bell, B.P. LeBlanc, E. Mazzucato, D.R. Smith, C.W. Domier and H. Yuh, "Exploring the regime of validity of global gyrokinetic simulations with spherical tokamak plasmas", Nucl. Fusion **60**, 026005 (2020).

[30] J. McClenaghan et. al., "Role of parallel magnetic field effects in predicting turbulent transport in NSTX", Plasma Phys. Control. Fusion **67**, 055013 (2025).

[31] B.S. Patel, M.R. Hardman, D. Kennedy, M. Giacomin, D. Dickinson and C.M. Roach, "The impact of $\vec{E}\times\vec{B}$ shear on microtearing based transport in spherical tokamaks", Nucl. Fusion **65**, 026063 (2025).

[32] J. Dominski, W. Guttenfelder, D. Hatch, T. Görler, F. Jenko, S. Munaretto, and S. Kaye, "Global micro-tearing modes in the wide pedestal of an NSTX plasma", Phys. Plasmas **31**, 044501 (2024).

[33] H. Chung, C.Y. Lee, G.J. Choi, S.M. Kaye, B.P. LeBlanc, J.W. Berkery and Y.-S. Na, "Development of a data-driven neural network model for electron thermal transport in NSTX", Nucl. Fusion **65**, 086028 (2025).

[34] T. Rafiq, J. Weiland, A.H. Kritz, L. Luo, and A.Y. Pankin, "Microtearing modes in tokamak discharges", Phys. Plasmas **23**, 062507 (2016).

[35] J. Candy, E.A. Belli, R.V. Bravenec, "A high-accuracy Eulerian gyrokinetic solver for collisional plasmas", J. Comput. Phys. **324**, 73 (2016).

[36] R.L. Miller, M.S. Chu, J.M. Greene, Y.R. Lin-Liu, R.E. Waltz, "Noncircular, finite aspect ratio, local equilibrium model", Phys. Plasmas **5**, 973-978 (1998).

[37] R. Arbon, J. Candy and E.A. Belli, "Rapidly-convergent flux-surface shape parameterization", Plasma Phys. Control. Fusion **63**, 012001 (2020).

[38] T. Rafiq, C. Wilson, C. Clauser, E. Schuster, J. Weiland, J. Anderson, S.M. Kaye, A. Pankin, B.P. LeBlanc and R.E. Bell, "Predictive modeling of NSTX discharges with the updated multi-mode anomalous transport module", Nucl. Fusion **64**, 076024 (2024).

[39] C.F. Clauser, W. Guttenfelder, T. Rafiq, and E. Schuster, "Linear ion-scale microstability analysis of high and low-collisionality NSTX discharges and NSTX-U projections", Phys. Plasmas **29**, 102303 (2022).

[40] C.F. Clauser, T. Rafiq, J. Parisi, G. Avdeeva, W. Guttenfelder, E. Schuster, C. Wilson, "Electron temperature gradient instability and transport analysis in NSTX and NSTX-U plasmas", Phys.

Plasmas **32**, 022305 (2025).
[41] R.V. Bravenec, J. Candy, M. Barnes, C. Holland, "Linear and nonlinear verification of gyrokinetic microstability codes", Phys. Plasmas **18**, 122505 (2011).
[42] J.F. Drake and Y.C. Lee, "Nonlinear evolution of collisionless and semicollisional tearing modes", Phys. Rev. Lett. **39**, 453 (1977).
[43] H. Doerk, F. Jenko, T. Görler, D. Told, M.J. Pueschel, and D.R. Hatch, "Gyrokinetic prediction of microtearing turbulence in standard tokamaks", Phys. Rev. Plasmas **19**, 055907 (2012).
[44] T. Singh, J.H. Nicolau, F. Nespoli, G. Motojima, Z. Lin, A. Sen, S. Sharma, and A. Kuley, "Global gyrokinetic simulations of electrostatic microturbulent transport in LHD stellarator with boron impurity", Nucl. Fusion **64**, 016007 (2024).
[45] T. Singh, K. Shah, D. Sharma, J. Ghosh, K.A. Jadeja, R.L. Tanna, M.B. Chowdhuri, Z. Lin, A. Sen, S. Sharma, and A. Kuley, "Gyrokinetic simulations of electrostatic microturbulence in ADITYA-U tokamak with argon impurity", Nucl. Fusion **64**, 086038 (2024).
[46] R.J. Hawryluk et al., "An empirical approach to tokamak transport", Physics of Plasmas Close to Thermonuclear Conditions Ed B. Coppi et al. (Brussels: CEC) **1**, 19–46 (1980).
[47] T.J. Martin, J.B. Taylor, "Ergodic behaviour in magnetic limiter", Plasma Phys. Control. Fusion **26**, 321 (1984).
[48] A.B. Rechester, M.N. Rosenbluth, "Electron heat transport in a tokamak with destroyed magnetic surfaces", Phys. Rev. Lett. **40**, 38 (1978).
[49] J. Wesson and D.J. Campbell, "Tokamaks", Oxford University Press **149** (2011).
[50] W.M. Nevins, E. Wang, and J. Candy, "Magnetic stochasticity in gyrokinetic simulations of plasma microturbulence", Phys. Rev. Lett. **106**, 065003 (2011).
[51] M.J. Pueschel, D.R. Hatch, M. Kotschenreuther, A. Ishizawa and G. Merlo, "Multi-scale interactions of microtearing turbulence in the tokamak pedestal", Nucl. Fusion **60**, 124005 (2020).
[52] T. Singh, J.H. Nicolau, Z. Lin, S. Sharma, A. Sen, and A. Kuley, "Global gyrokinetic simulations of electrostatic microturbulent transport using kinetic electrons in LHD stellarator", Nucl. Fusion **62**, 126006 (2022).
[53] D.R. Hatch, M. Kotschenreuther, S. Mahajan, P. Valanju, F. Jenko, D. Told, T. Görler and S. Saarelma,"Microtearing turbulence limiting the JET-ILW pedestal", Nucl. Fusion **56**, 104003 (2016).
[54] T. Singh, T. Rafiq, E. Schuster, Z. Lin, E. Schuster, "Global gyrokinetic simulations of kinetic ballooning mode in NSTX-U plasmas", Nucl. Fusion **65**, 106039 (2025).
[55] D. Kennedy et al., "A tale of two (visco)cities: Electromagnetic turbulence and transport bifurcations: Implications for next-generation fusion power plants", Nucl. Fusion *submitted* (2025).
[56] M. Giacomin, D. Kennedy, F.J. Casson, Ajay C.J., D. Dickinson, B.S. Patel and C.M. Roach, "On electromagnetic turbulence and transport in STEP", Plasma Phys. Control. Fusion **66**, 055010 (2024).
[57] E.A. Belli and J. Candy, "Kinetic calculation of neoclassical transport including self-consistent electron and impurity dynamics", Plasma Phys. Control. Fusion **50**, 095010 (2008).
[58] K.L. Wong, S. Kaye, D.R. Mikkelsen, J.A. Krommes, K. Hill, R. Bell, B. LeBlanc, "A quantitative account of electron energy transport in a National Spherical Tokamak Experiment plasma", Phys. Plasmas **15**, 056108 (2008).
[59] E.A. Belli, J. Candy,, "Implications of advanced collision operators for gyrokinetic simulation", Plasma Phys. Control. Fusion **59**, 045005 (2017).
[60] T. Singh, D. Sharma, T. Macwan, S. Sharma, J. Ghosh, A. Sen, Z. Lin and A. Kuley, "Gyrokinetic simulations of electrostatic microturbulence in ADITYA-U tokamak", Nucl. Fusion **63**, 056008 (2023).
[61] E.A. Belli, J. Candy, I. Sfiligoi and W. Guttenfelder, "Separability of microtearing mode and electron temperature gradient turbulence regimes", Plasma Phys. Control. Fusion **67**, 105015

(2025).
[62] Z. Lin, T.S. Hahm, W.W. Lee, W.M. Tang, and P.H. Diamond, "Effects of collisional zonal flow damping on turbulent transport", Phys. Rev. Lett. **83**, 3645 (1999).
[63] M.N. Rosenbluth and F.L. Hinton, "Poloidal flow driven by ion-temperature-gradient turbulence in tokamaks", Phys. Rev. Lett. **80**, 724 (1998).